U.S. Department of Energy
Energy Efficiency and Renewable Energy
Bringing you a prosperous future where energy is clean, abundant, reliable, and affordable

Industrial Technologies Program
Industrial Materials for the Future

Final Technical Report

Development of Combinatorial Methods for Alloy Design and Optimization

June 2006

Principal Investigators:

George M. Pharr
University of Tennessee

Easo P. George
Michael L. Santella
Oak Ridge National Laboratory

UT
University of Tennessee

ORNL
OAK RIDGE NATIONAL LABORATORY

**Managed by
UT-Battelle, LLC**

ORNL/TM-2005/133

FINAL TECHNICAL REPORT

Project Title: Development of Combinatorial Methods for Alloy Design and Optimization

Award Number: DE-FC36-02ID14251

Project Period: April 1, 2002–March 31, 2005

Principal Investigator: Professor George M. Pharr
(865) 974-8202
pharr@utk.edu

Additional Investigators: Dr. Easo P. George (ORNL; georgeep@ornl.gov)
Dr. Michael L. Santella (ORNL; santellaml@ornl.gov)

Recipient Organization: University of Tennessee
404 Andy Holt Tower
Knoxville, TN 37996-0140

Industrial Partner: Duraloy Technologies, Inc.

Development of Combinatorial Methods for Alloy Design and Optimization

George M. Pharr, Easo P. George, Michael L. Santella

June 2006

Acknowledgments and Disclaimer

Acknowledgments

Disclaimer

Contents

List of Figures

Abbreviations and Acronyms

AES   Auger electron spectroscopy/spectroscope
ANL   Argonne National Laboratory
APS   Advanced Photon Source
bcc   body-centered cubic
BSE   backscattered electron
CCD   charge-coupled device
EB   electron beam
EBW   electron-beam welding
EDS   energy-dispersive spectroscopy/spectroscope
fcc   face-centered cubic
IMF   Industrial Materials for the Future
ORNL   Oak Ridge National Laboratory
PIN   positive-intrinsic-negative
PVD   physical vapor deposition
SEM   scanning electron microscopy/microscope
XRD   X-ray diffraction
XRF   X-ray fluorescence

1. Executive Summary

The primary goal of this research, which was sponsored under the Knowledge Base or Core Activities category of IMF solicitation DE-PS07-01ID14123, was to develop a comprehensive methodology for designing and optimizing metallic alloys by combinatorial principles. Because conventional techniques for alloy preparation are unavoidably restrictive in the range of alloy composition that can be examined, combinatorial methods promise to significantly reduce the time, energy, and expense needed for alloy design. Combinatorial methods can be developed not only to optimize existing alloys, but to explore and develop new ones as well.

The scientific approach involved fabricating an alloy specimen with a continuous distribution of binary and ternary alloy compositions across its surface—an "alloy library"—and then using spatially resolved probing techniques to characterize its structure, composition, and relevant properties. The three specific objectives of the project were (1) to devise means by which simple test specimens with a library of alloy compositions spanning the range of interest can be produced; (2) to assess how well the properties of the combinatorial specimen reproduce those of the conventionally processed alloys; and (3) to devise screening tools which can be used to rapidly assess the important properties of the alloys. As proof of principle, the methodology was applied to the Fe-Ni-Cr ternary alloy system that constitutes many commercially important materials such as stainless steels and the H-series and C-series heat- and corrosion-resistant casting alloys.

Three different techniques were developed for making alloy libraries: (1) vapor deposition of discrete thin films on an appropriate substrate followed by use of solid-state diffusion to alloy film and substrate together; (2) co-deposition of the alloying elements from three separate magnetron sputtering sources onto an inert substrate; and (3) localized melting of thin films with a focused electron-beam welding (EBW) system. Each of the techniques was found to have its own advantages and disadvantages.

A new and very powerful technique for rapid structural and chemical characterization of alloy libraries was developed on the basis of high-intensity X-radiation available at synchrotron sources such as the Advanced Photon Source (APS) at Argonne National Laboratory (ANL). With the technique, structural and chemical characterization of up to 2500 discrete positions on a library can made in less than 4 h. Among the parameters that can be measured are the chemical composition, crystal structure, lattice parameters, texture, and grain size. From these, one can also deduce isothermal sections of ternary phase diagrams. The equipment and techniques needed to do this are now in place for use in future combinatorial studies at the Oak Ridge National Laboratory (ORNL) beam line at the APS.

In conjunction with the chemical and structural investigations, nanoindentation techniques were developed to investigate the mechanical properties of the combinatorial libraries. The two primary mechanical properties of interest were the elastic modulus, E, and hardness, H, both of which were measured on alloy library surfaces with spatial resolutions of better than 1 μm. A nanoindentation testing system at ORNL was programmed to make a series of indentations at specified locations on the library surface and automatically collect and store all the data needed to obtain hardness and modulus as a function of position. Approximately 200 indentations can be made during an overnight run; this capability provides mechanical property measurements over a wide range of chemical compositions in a relatively short time.

Since the materials based on the Fe-Ni-Cr system often find application in highly carburizing and harsh chemical environments, simple techniques were developed to assess the resistance of Fe-Ni-Cr alloy libraries to carburization and corrosion. Alloy libraries were carburized by standard techniques, and the effectiveness of the carburization at various points along the sample surface was assessed by nanoindentation hardness measurement. Corrosion tests were conducted by placing library specimens in highly corrosive aqueous environments, with the corrosion resistance assessed using surface profilometry to measure the local surface recession relative to inert markers.

Collectively, the suite of newly developed tools and techniques paves the way for combinatorial design, discovery, and optimization of a wide variety of alloys, thus leading to improved materials in manner that crosscuts the needs of a large number of energy-intensive industries. Among those that would be directly impacted are aluminum, chemicals, forest products, glass, metal casting, petroleum, steel, forging, heat treating, and welding.

2. Introduction

Combinatorial materials science is a relatively new field that uses combinatorial methods to identify important new materials for use in engineering applications [1–12]. This emerging technology has evolved from techniques developed primarily by the U.S. chemical and pharmaceutical industries to identify promising new compounds based on the rapid synthesis and evaluation of a large number of materials. In the 1990s, combinatorial methods were adopted by materials scientists to search for and optimize new engineering materials for a wide variety of applications. Although still in its infancy, combinatorial materials science has been successfully employed to discover a host of new materials for photoluminescence, catalysis, and superconductivity, as well as for applications involving dielectric, magnetic, and ferroelectric materials.

The high-throughput screening for new drugs and biomolecules that is now possible with the help of combinatorial chemistry has already revolutionized the pharmaceutical and biotechnology industries [1–3]. Combinatorial methods have also been used in the development and discovery of new chemical compounds with technological applications in photoluminescent phosphors, metal-organic catalysts, and superconductors [1–3]. While these examples of the successful use of combinatorial techniques are all limited to organic and inorganic chemistry, there is increasing interest in applying the basic principles of high-throughput and combinatorial techniques in the search for, and optimization of, new materials in other fields. According to an article in the journal *Science* [12], further advances in this area will benefit a whole host of U.S. industries.

The basic principles of combinatorial chemistry also have much to offer in the field of materials science. For example, current techniques for preparing metallic alloys unavoidably restrict us to narrow ranges of alloy composition. Combinatorial methods promise to enhance significantly the composition range that can be explored, thereby leading to the discovery of important *new* materials. Combinatorial methods will also be useful in optimizing *existing* alloys. Because of the time and expense of qualifying engineering materials, the industrial approach often is to tweak existing alloys to improve their properties rather than to develop new alloys. Examples of recent alloy optimization programs at ORNL include work with Teledyne Allvac on P and B additions in alloy 718 and Waspaloy to improve creep-rupture properties [13–15]; work with Siemens-Westinghouse on control of Zr, B, and S in IN 939 to improve its weldability for use in land-based gas turbines [16]; and work with Ford and Wescast to modify the composition of ductile cast iron so that it can be used at higher temperatures in next-generation exhaust manifolds. In all of these alloy optimization projects, the combinatorial approach would be an invaluable screening tool that could dramatically shorten the time needed to investigate the various alloy compositions. Also, a wider range of composition space could be explored, possibly leading to better alloys.

To this end, the work described in this report was aimed at developing combinatorial methods that will be useful in the design and optimization of metallic alloys. While this initial study was limited to one simple model metallic system, the techniques are applicable to a wide variety of alloys and will thus lead to improved materials in a manner that crosscuts the needs of a large number of IMF industries that rely upon them. Among the industries that would be directly impacted are aluminum, chemicals, forest products, glass, metal casting, petroleum, steel, forging, heat treating, and welding. In addition, the general principles developed here have the potential to expand into a large multidisciplinary effort that could provide a new way of studying composition-structure-property relationships in materials other than metallic alloys, thereby resulting in the discovery of a host of new materials with useful and possibly unexpected properties. Among the research areas where we foresee potential application are superconductivity, electromigration, catalysis, radiation damage,

refractory metal alloy development, shape memory effects, magnetic thin films, blended polymers, thermoelectric materials, functional gradient materials, flat panel display materials, and layered ceramics.

3. Program Goals and Objectives

The primary goal of this research program was to develop a comprehensive methodology for designing and optimizing metallic alloys by combinatorial principles. This was accomplished by developing techniques that can be used to fabricate an alloy specimen with a continuous distribution of binary and ternary alloy compositions across its surface—an "alloy library"—and then using spatially resolved probing techniques to characterize the structure, composition, and relevant properties of the library. Three specific objectives were to

1. devise means by which simple test specimens with a library of alloy compositions spanning the range of interest can be produced;

2. assess how well the properties of the combinatorial specimen reproduce those of the conventionally processed alloys; and

3. devise screening tools that can be used to rapidly assess important alloy properties.

As proof of principle, the methodology was applied to the Fe-Ni-Cr ternary alloy system that constitutes many commercially important materials such as stainless steels and the H-series and C-series heat- and corrosion-resistant casting alloys. Applying the techniques to this and other alloy systems in future work will result in significant, energy, environmental, and economic benefits.

Three different techniques for producing alloy libraries were developed: (1) vapor deposition of discrete thin films on an appropriate substrate followed by use of solid-state diffusion to alloy film and substrate together; (2) co-deposition of alloying species from three separate magnetron sputtering sources onto an inert substrate; and (3) localized melting of thin films with a focused EB welding system.

A new and very powerful technique for structural and chemical characterization is based on high-intensity X-radiation available at synchrotron sources such as the APS. With this technique, structural and chemical characterization of up to 2500 discrete positions in an alloy library can made in less than 4 h. Among the measurements that can be made are chemical composition, crystal structure, lattice parameters, texture, and grain size. From these, one can deduce isothermal sections of ternary phase diagrams. The equipment and techniques needed to do this are now in place for use in future combinatorial studies at the ORNL beam line at the APS.

In conjunction with the chemical and structural investigations, nanoindentation techniques were developed to investigate the mechanical properties of the combinatorial libraries. The two primary mechanical properties of interest were the elastic modulus, E, and hardness, H, both of which were measured on alloy library surfaces with spatial resolutions of better than 1 µm. A nanoindentation testing system at ORNL was programmed to make a series of indentations at specified locations on the alloy library surface and automatically collect and store all the data needed to obtain hardness and modulus as a function of position on the combinatorial sample surface. Approximately 200 indentations can be made during an overnight run; this capability provides mechanical property measurements over a wide range of chemical compositions in a relatively short time.

Since the materials based on the Fe-Ni-Cr system often find application in highly carburizing and harsh chemical environments, simple techniques were developed to assess the resistance of the ternary Fe-Ni-Cr alloy libraries to carburization and corrosion. Alloy libraries were carburized, and

the effectiveness of the carburization at various points along the sample surface was assessed by nanoindentation hardness measurement. Corrosion tests were conducted by placing library specimens in highly corrosive aqueous environments, with the corrosion susceptibility assessed using surface profilometery to establish the local surface recession relative to inert markers.

Each of these techniques and their relative advantages and disadvantages are detailed in the following section.

4. Technical Accomplishments, Results, and Discussion

4.1 Rapid Chemical and Structural Characterization by Synchrotron X-ray Diffraction

We begin the technical discussion by detailing the synchrotron-based methods developed for rapid chemical and structural characterization of alloy libraries. Because these methods proved invaluable in assessing the methods for alloy library preparation, it is useful to have an understanding of them before describing the library preparation techniques.

The chemical and structural characterization techniques were developed using Fe-Ni-Cr alloy libraries prepared by thin film deposition. Details will be given later, but in brief, sequential layers of Fe, Ni, and Cr were deposited on (0001) sapphire substrates 50 mm in diameter by electron beam evaporation in a vacuum of 10^{-6} to 10^{-7} torr. The average deposition rate was ~1 nm/s, as measured with a gold-coated quartz crystal resonator operating at 6 MHz. Each layer was grown with a linear thickness gradient by sliding a stepping motor-driven shutter located between the specimen and the evaporation target. After a layer was deposited, the sample was rotated 120° for deposition of the next layer. This resulted in a triangular region with an elemental distribution close to that of the composition triangle of a standard ternary phase diagram. The order of the layers and the maximum thickness of each layer are listed in Table 1. The layers were alloyed by annealing at ~850°C in a vacuum of 5×10^{-7} torr. The heating time and heating conditions required to interdiffuse the layers were estimated and confirmed by angular-resolved X-ray fluorescence (XRF) and cross-sectional scanning electron microscopy (SEM) with energy-dispersive X-ray spectroscopy (EDS).

Table 1. Sample specifications

Sample	Layers	Annealing conditions
A	Ni(1.85 µm)/Fe(1.6 µm)/Cr(1.7 µm)/Al$_2$O$_3$(0001)	20 h, 850°C, vacuum
B	Ni(2.0 µm)/Fe(2.5 µm)/Cr(2.5 µm)/Al$_2$O$_3$(0001)	2 h, 825°C, vacuum
C	Ni(0.74 µm)/Fe(1.7 µm)/Cr(1.56 µm)/Al$_2$O$_3$(0001)	20 h, 850°C, vacuum

As shown schematically in Fig. 1, X-ray diffraction and fluorescence data were collected at beamline 33-ID-D of the APS. Undulator radiation, monochromatized to 15 keV by Si(111) crystals and focused to ~0.25×0.5 mm^2, was incident on the sample at a 15° glancing angle, giving a 1.0×0.5 mm^2 footprint on the sample. The incident beam was filtered with a 0.25-mm Ti foil (1.7% transmission) to avoid saturating the detectors. The sample was mounted on a five-axis translation/ rotation system consisting of a raster motion transverse to the incident beam, a rotation to set the glancing angle, a raster motion in the plane of the sample along the beam, and two tilts to align the sample plane with the plane spanned by the raster motions.

The incident beam intensity was monitored with an air-filled ion chamber. Diffraction patterns were recorded by a 1024×1024 charge-coupled device (CCD) X-ray camera with 60 µm pitch, located 10 cm behind the sample. Fluorescence was measured by a thermoelectrically cooled silicon positive-intrinsic-negative (PIN) photodiode, with the Cr, Fe, and Ni K$_\alpha$ intensities each recorded using a single-channel analyzer. The sample was rastered on a 1×1 mm^2 grid, with a set of data collected at each point at 7-s intervals. Data was collected for the entire circular substrate in 4 h, of which
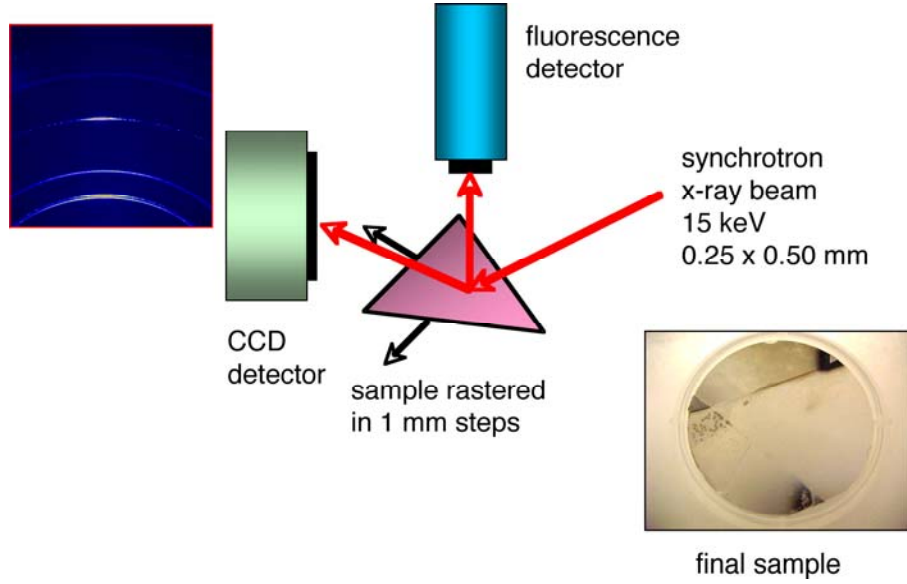
Fig. 1. Schematic illustration of system assembled at the Advanced Photon Source (APS) for rapid chemical and structural characterization of combinatorial libraries.

2 h was spent scanning the triangular ternary system—that is, data collection time could be halved by carefully defining the area to be scanned.

The fluorescent intensities at each point on the samples were used to find the elemental compositions. Because of the limited energy resolution of the photodiode, there were peak overlaps: chromium K_β radiation produced a signal on the iron K_α channel and iron K_β on Ni K_α. Overlaps were measured using the pure metal corners of the specimen and were accounted for by subtracting an appropriate fraction of the chromium and iron signals from those of iron and nickel, respectively. The corrected fluorescence F_A from element A was related to the densities c_B of each element B by

$$F_A = d_a I \int_0^T \exp\left(-\frac{z\sum_B \sigma_B c_B}{\sin\theta} - \frac{z\sum_B \sigma'_B c_B}{\sin\theta'} \right), \tag{1}$$

where I is the incident beam intensity, T is the film thickness, σ_B and σ'_B are the absorption cross sections for incident and fluorescent X-rays by element B, and $\Theta = 15°$ and $\Theta' = 56°$ are the glancing angles for incident and fluorescent X-rays. The constants d_A for each element—which depend on the fluorescence cross section, absorption by air, and the efficiency of the detectors for incident and fluorescent X-rays—were found by measuring fluorescence from the pure elements. Ratios of the fluorescence intensities at each point can be measured more accurately than the absolute intensities because the ratios are not affected by dead time in the detectors or by dark current in the incident-beam monitor, so at each point least-squares refinement was used to find the ratios $c_A/\Sigma_B c_B$ which give a best fit to the measured ratios $F_A/\Sigma_B F_B$, subject to the constraint that $\Sigma_B c_B = c_t$; we approximate $c_t = 8.65 \times 10^{22}/\text{cm}^3$.

Diffraction patterns were analyzed using the FIT2D package [17,18]. A diffraction pattern from a standard polycrystalline Al_2O_3 sample (NIST SRM 1976) was used to find the sample–CCD distance and direct beam location on the CCD. The two-dimensional images were then integrated without

further correction to yield one-dimensional scans of intensity versus plane spacing. Composite two-dimensional images were constructed in which each row corresponded to one integrated diffraction pattern; phase boundaries were visible on these composite images. Quantitative analyses of lattice parameters and peak intensities were performed by least-squares fitting to one-dimensional scans. Lattice parameters were sensitive to sample displacements: a displacement of 0.1 mm was calculated to cause an error of ~0.2% in lattice parameter. A linear correction was made to lattice parameters to match the bulk value for pure elements at the corners of the phase diagram to correct for sample displacement and tilt. This calibration procedure also removed the effects of residual stress (caused by differential thermal expansion between the substrate and film), assuming that the strain is uniform across the ternary section.

The techniques were used to fully characterize the structure and composition of ternary alloy films annealed at ~850°C, from which isothermal sections of the phase diagram and contour maps of lattice parameters were constructed. Approximately 2500 compositions were examined in a single experiment taking ~4 h.

The measured elemental composition of sample A is shown in Fig. 2. Lines are contours of 0, 10, … , 90 at. % Cr, Fe, and Ni. Small deviations from the intended linear composition profiles are visible and are corrected for in the ternary phase diagrams that follow. Similar corrections were made for the other samples.

A typical CCD image is shown in Fig. 3, including an epitaxial body-centered cubic (bcc) phase and a weakly textured face-centered cubic (fcc) phase. Because the bcc phase is so much better aligned, it scatters much more strongly at its peak, and a conventional $\Theta/2\Theta$ scan incorrectly indicates that the fcc is a trace phase relative to the bcc, as would a scan taken with a linear detector. Integrating the CCD image correctly shows that both are major components.

Integrated powder patterns for the various phases are shown in Fig. 4. We observed three equilibrium phases in the Cr–Fe–Ni system. The bcc or α phase is the structure of iron and chromium, and the fcc or γ phase is that of nickel. A tetragonal intermetallic σ phase occurs as the metals approach the $Cr_{50}Fe_{50}$ composition. Cr_2O_3 can be seen in the chromium-rich compositions due to residual oxygen during annealing.
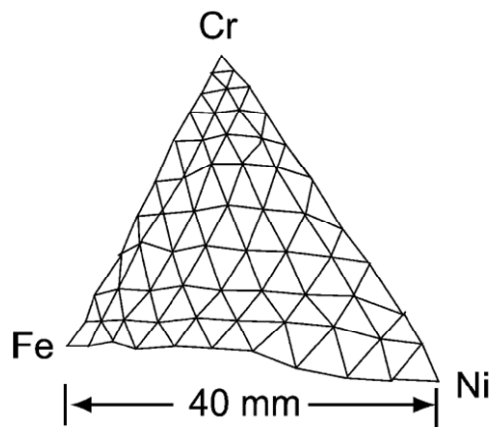
Fig. 2. Geometrical locations of the ternary composition grid on sample A. Lines are contours of 0, 10, . . . , 90 at. % Cr, Fe, and Ni.

9
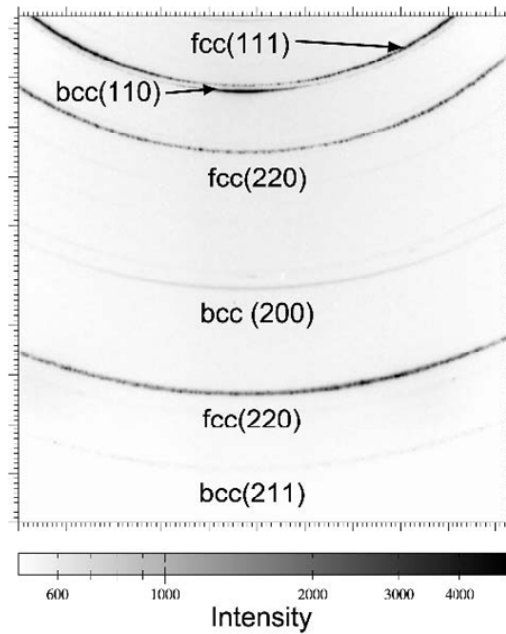
Fig. 3. CCD image from $Fe_{10}Cr_{60}Ni_{30}$ on sample A, illustrating a weakly textured fcc phase and a bcc phase with (110) epitaxy. Weak, unlabeled peaks are from Cr_2O_3. Note the log scale: the bcc (110) scattering is 50 times as intense as the bcc (200).
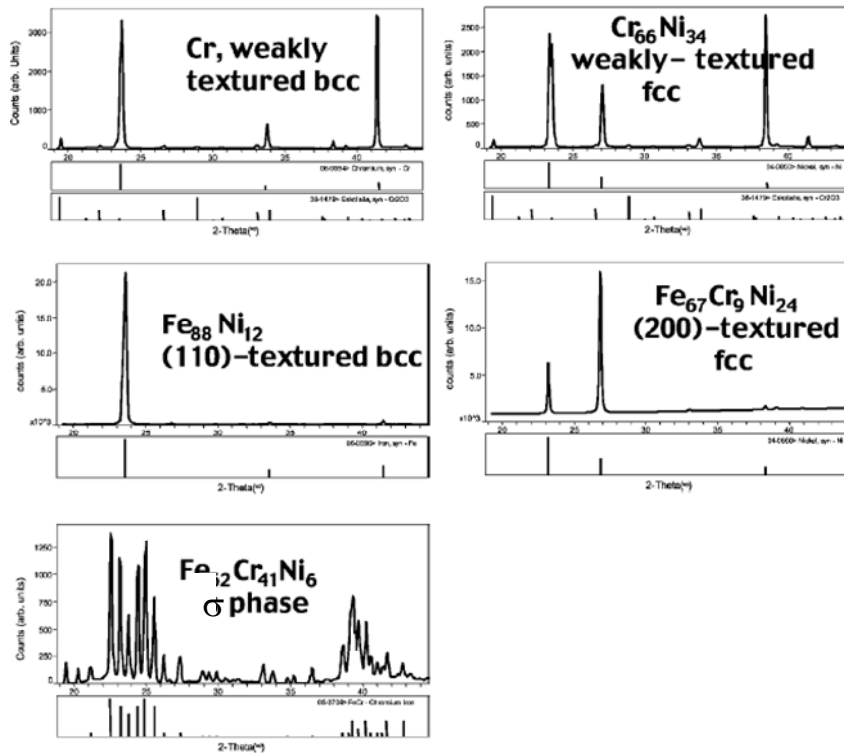
Fig. 4. Integrated powder patterns for phases occurring in sample A.

10

The relative peak intensities show the crystallographic texture. For a randomly oriented film, the relative peak intensities would be the same as for a random powder; deviations are due to preferred orientation. Pole figures using a conventional X-ray system show that the highly textured phases are in fact fully epitaxial. The bcc phase is weakly textured except for compositions near pure iron, where it is epitaxial with bcc (110) parallel to Al_2O_3 (0001) and bcc <110> parallel to Al_2O_3 <11$\overline{2}$0> or <10$\overline{1}$0>. The fcc phase is weakly textured at high chromium concentrations, while at low chromium concentrations it is epitaxial with fcc (110) parallel to Al_2O_3 (0001) with poorer alignment than the epitaxial bcc phase. The σ phase is randomly oriented.

A composite image of 49 scans, forming one row along the sample, is shown in Fig. 5, illustrating the appearance of the various phases. The identification of phase boundaries was not automated, in part because of the complication of epitaxy: various diffraction lines may be either missing or very intense, depending on the alignment of the film. We observed that growth on the (11$\overline{2}$3) surface of Al_2O_3 produces films with much more random alignment. Use of this surface may permit automation of this tedious step.

Ternary phase diagram sections for the three samples have been assembled and are shown in Fig. 6 along with the known equilibrium phase diagram section for 850°C [19]. The agreement is generally good. The least-annealed sample, B, has a larger three-phase region than the calculated section and no
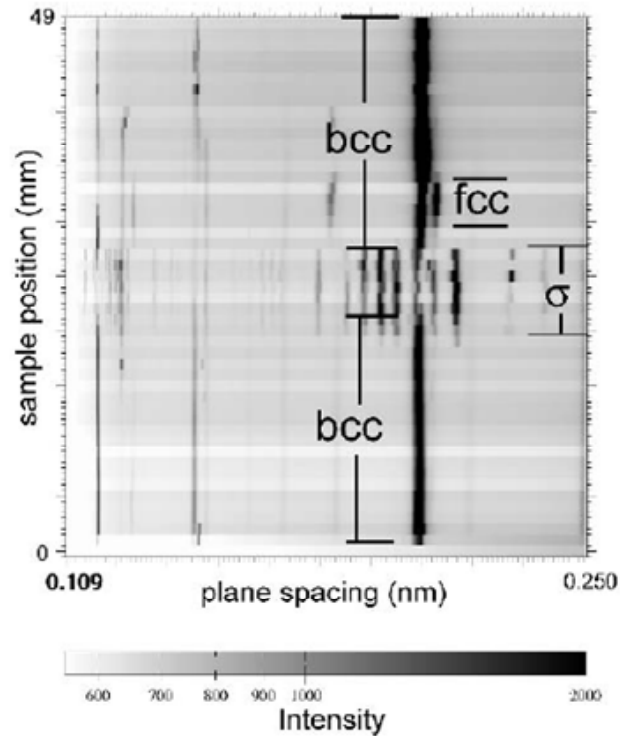
Fig. 5. Composite image of 49 scans. Each row of the composite corresponds to an integrated CCD image from sample A as it is translated under the X-ray beam in one line of the raster pattern covering the entire sample. The ranges over which each phase is observed are indicated. Weak, unlabeled lines are due to Cr_2O_3.
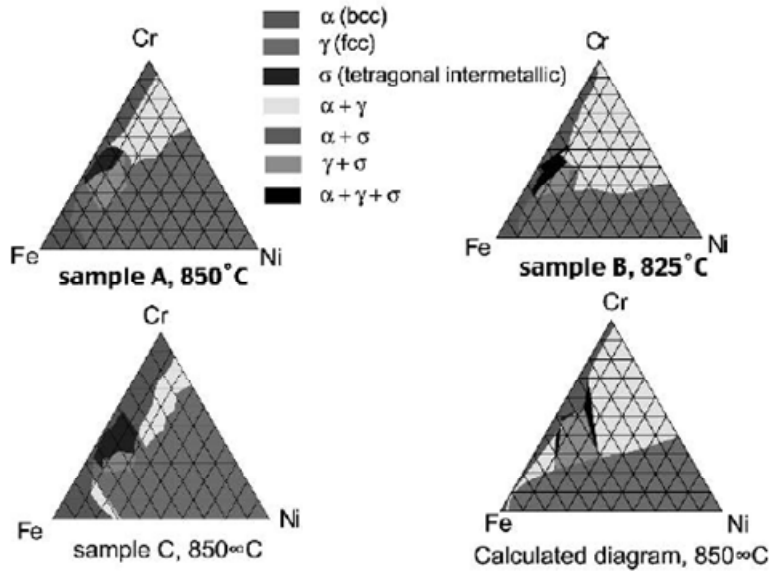
Fig. 6. Measured phase diagram sections compared to that calculated by Chuang and Chang [19].

single-phase σ region. This is to be expected for an under-annealed sample because the samples are all grown as laminates of bcc and fcc phases and become single phase only by interdiffusion. The more-annealed samples, A and C, show fcc single-phase regions extending much further into the chromium-rich area than expected. This is to be expected from the unintended oxidation of these samples. Cr_2O_3 is observed to form on the chromium-rich material, leaving the metal deficient in chromium. The phase boundary will therefore be at a composition with less chromium than indicated by the fluorescence measurement. A and C were deposited with different layer sequences but still yield similar phase diagram sections, which suggests that these are indeed equilibrium results. Abrupt transitions from single-phase α to σ confirm that the measurement achieves resolution of 2 at. %.

There is no significant variation in the lattice parameter of the bcc or σ phases. The lattice parameter for the fcc phase, calculated from the (200) reflection of sample A, is shown in Fig. 7, along with the results obtained by conventional methods [20]. The agreement is generally good, although some artifacts can be seen along the line of zero chromium concentration, presumably due to starting of the
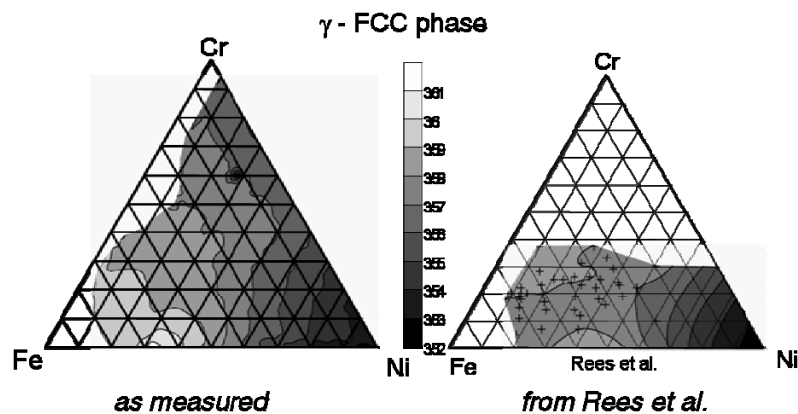
Fig. 7. Lattice parameter from fcc (200) reflection from sample A compared to results of Rees, Burns, and Cook [20].

12

shutter motion. As expected, lines of constant lattice parameters follow tie lines across the two-phase fcc-bcc region.

The results of this study clearly demonstrate the power of this new combinatorial technique for rapid structural and chemical characterization. A combinatorial library spanning the entire Cr–Fe–Ni ternary system was measured at 2500 different positions in just 4 h at a resolution of 2 at. %. The measurements were used to determine the local chemical composition, crystallographic phases, texture, lattice parameters, and ternary phase diagram. The technique is now fully implemented on the ORNL beamline at the APS and is available for future combinatorial materials design efforts.

4.2 Preparation of Alloy Libraries by Thin Film Deposition and Interdiffusion

The first method developed for preparing combinatorial alloy libraries was based on thin film deposition and interdiffusion of the discrete layers of the component materials by annealing. Specimens of Fe-Ni-Cr were prepared by depositing films onto 5-cm-diam circular sapphire substrates, followed by annealing in vacuum to interdiffuse the layers. Substrates with three different orientations were used: (0001), $(11\bar{2}0)$, and $(1\bar{1}02)$. The last two orientations were found to suppress texture formation and therefore simplify structural analysis by X-ray diffraction (XRD).

Deposition was performed in an electron beam evaporation system equipped with a sliding shutter and a sample rotation stage like that shown in Fig. 8. A typical background pressure was ~10^{-6} torr, with the deposition rate measured using a quartz crystal resonator being ~3 nm/s for chromium
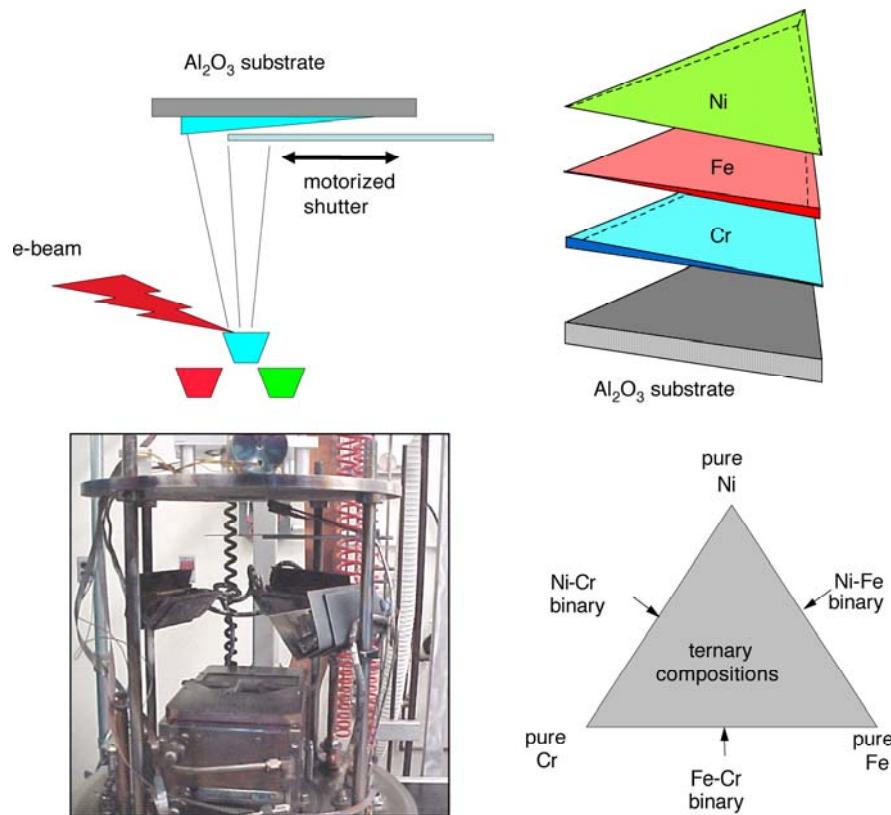
Fig. 8. A schematic diagram of the deposition process used to make thin film libraries by thin film deposition and annealing.

13

and ~0.3 nm/s for iron and nickel. Layers of Cr, Fe, and Ni were sequentially deposited using a sliding shutter to create a thickness gradient in each layer. The shutter was moved at a constant rate such that the thicknesses increased linearly with position to a maximum of ~1.7 μm on the thick end. After a layer was finished, the sample was rotated by 120° about the substrate center, and a layer of a different alloying component was deposited. The total thickness of the deposited layers was limited by the maximum thickness measurable by the quartz crystal resonator (~5 μm).

After deposition, the layers were interdiffused by annealing in a vacuum using annealing times and temperatures described below. After annealing, the sample was slowly cooled to room temperature in ~12 h, with the initial cooling to 500°C taking ~1 h. The resulting sample had a triangular region with a constant thickness of ~1.7 μm and unmixed compositions spanning the entire ternary phase diagram. Monolithic films of Fe, Cr, and Ni with uniform layer thicknesses of ~1.7 μm were also prepared to examine the extent of the interdiffusion during annealing.

The quality of the alloyed specimens was examined using cross-sectional SEM, angular resolved X-ray fluorescence (XRF), scanning Auger electron spectroscopy (AES), and XRD, including diffraction mapping using synchrotron radiation as described in the previous section. Samples for cross-sectional SEM were cut from the wafer, mounted in epoxy, polished, and carbon coated. Angular resolved XRF measurements were made with a rotating copper anode operated at 50 kV and 100 mA. Copper K_β radiation was employed using a sagitally focusing bent graphite monochromator. The angle of incidence, Θ, on the sample was varied from 2.5 to 35°, exciting fluorescence from the Cr, Fe, and Ni atoms in the sample. The fluorescence was analyzed using a lithium-drifted silicon detector in a symmetrical Θ-2Θ geometry—that is, the fluorescence detector was positioned to detect at a reflected angle equal to the angle of the incident X-ray beam. For a layer of uniform composition, this results in no variation of fluorescent intensity with changes in 2Θ (in the limit of a thick layer), while for a compositionally stratified layer, fluorescence from the near-surface region is stronger at smaller 2Θ. This was found to provide a useful way to explore the through-thickness homogeneity of the specimens after annealing.

Synchrotron-based structural and chemical mapping was conducted at the 33 BM beam line of the APS using 12-keV X-rays focused to give a 1-mm^2 footprint on the sample. The sample was rastered in the x-y plane of the sample with 1-mm steps to provide composition and structural information at each sample point. The structure was determined using diffracted X-rays collected with a 1024 × 1024 pixel CCD camera. The chemical composition was measured by XRF using a silicon detector. The area under each peak of the fluorescence spectrum was found by least-squares fitting to Gaussian line shapes. While the measurements were precise to within a 1% absolute variation in composition, the systematic error was estimated to be ~10%. The incident angle for diffraction and the takeoff angle for fluorescence were ~75° from the sample normal.

The most important requirement for the ternary alloy library specimens is complete through-thickness mixing of the metal layers. To achieve this mixing, we selected a temperature range of 825 to 875°C for annealing. At higher temperatures, chromium evaporation was significant, and for lower temperatures, delamination of the film from the substrate became a problem, as will be discussed later.

The time required for the layers to fully interdiffuse was first roughly estimated based on published diffusion data [21,22]. In the temperature range 825 to 875°C, typical diffusion coefficients for the Ni-Fe-Cr system are on the order of 10^{-16} m^{2}s^{-1}, which suggests that ~10 h is required for 1.7-μm films. Studies to establish the annealing conditions more precisely were conducted using specimens in which the Cr, Fe, and Ni layers were uniform. Each layer had a thickness of 1.7 μm, with the layer

closest to the substrate being chromium, followed by iron and nickel. For this composition, a homogeneous single fcc phase is expected at equilibrium.

Figure 9 shows typical cross-sectional SEM pictures of the "as deposited" sample [Fig. 9(a)] and the sample after annealing in vacuum at 825°C for 2 h 10 min [Fig. 9(b)] and 19 h 30 min [Fig. 9(c)]. In Fig. 9(a), all three as-deposited metal layers are distinguishable in the SEM image, and the interfaces between the layers are relatively flat. A gap between the substrate and the film formed as a result of film delamination due to epoxy shrinkage during mounting. A crack in the film may have been formed as a result of the internal film stress. After 2 h 10 min of annealing [Fig. 9(b)], the appearance of the layers changed dramatically. Two different areas separated by a gap are observed. Based on EDS measurements of the chemical constituents, the outer layer is a relatively uniform mixture of Fe-Ni-Cr, while the thin, rough inner layer on the substrate consists mainly of chromium oxide. The oxide, which presumably originates from oxygen dissolved in the film, oxygen introduced during annealing, and/or oxygen in the substrate, ties up some of the chromium and therefore reduces the local chromium concentration in the outer alloyed layer. The chromium oxide is well adhered to the substrate. The gap between the alloy and the chromium oxide was formed mainly as result of epoxy shrinkage. Note that although the inner surface of the alloy layer is relatively flat, the chromium oxide surface is extremely rough, suggesting some void formation during interdiffusion. Fig. 9(c) shows that the roughness and porosity of the outer Ni-Fe-Cr layer increases with annealing time. Thus, in order to obtain alloy libraries of high structural quality, very long annealing times should be avoided.
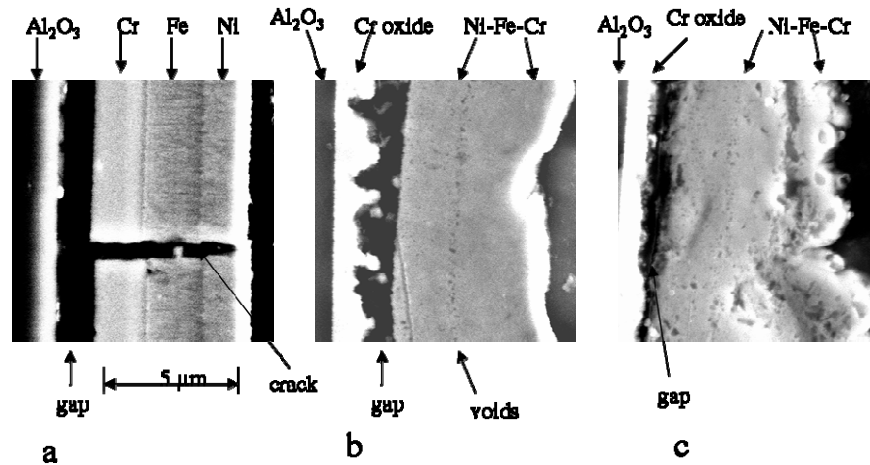
Fig. 9. Cross-sectional SEM images of Fe-Ni-Cr sample: (a) as deposited; (b) after annealing in vacuum at 825°C for 2 h 10 min; (c) after annealing in vacuum at 19 h 30 min.

The through-thickness chemical uniformity of the interdiffused layers was analyzed using angular resolved XRF. Typical results are shown in Fig. 10, which presents fluorescence spectra for an as-deposited specimen [Fig. 10(a)] and three specimens annealed in vacuum at 825°C for periods of 2 h 10 min [Fig. 10(b)], 5 h [Fig. 10(c)], and 19 h 10 min [Fig. 10(d)]. Each plot includes spectra obtained at $2\theta = 5°$, $10°$, and $70°$. For the specimens in Figs. 10(b) and 10(d), the pressure in the furnace prior to annealing was 7×10^{-7} torr. For the specimen in Fig. 10(c), the pressure was slightly higher at 6×10^{-6} torr.

The data in Fig. 10(a) illustrate the utility of the angular resolved fluorescence technique. For $2\theta = 5°$ and $10°$, no chromium or iron K_α peaks are observed because the chromium and iron are buried
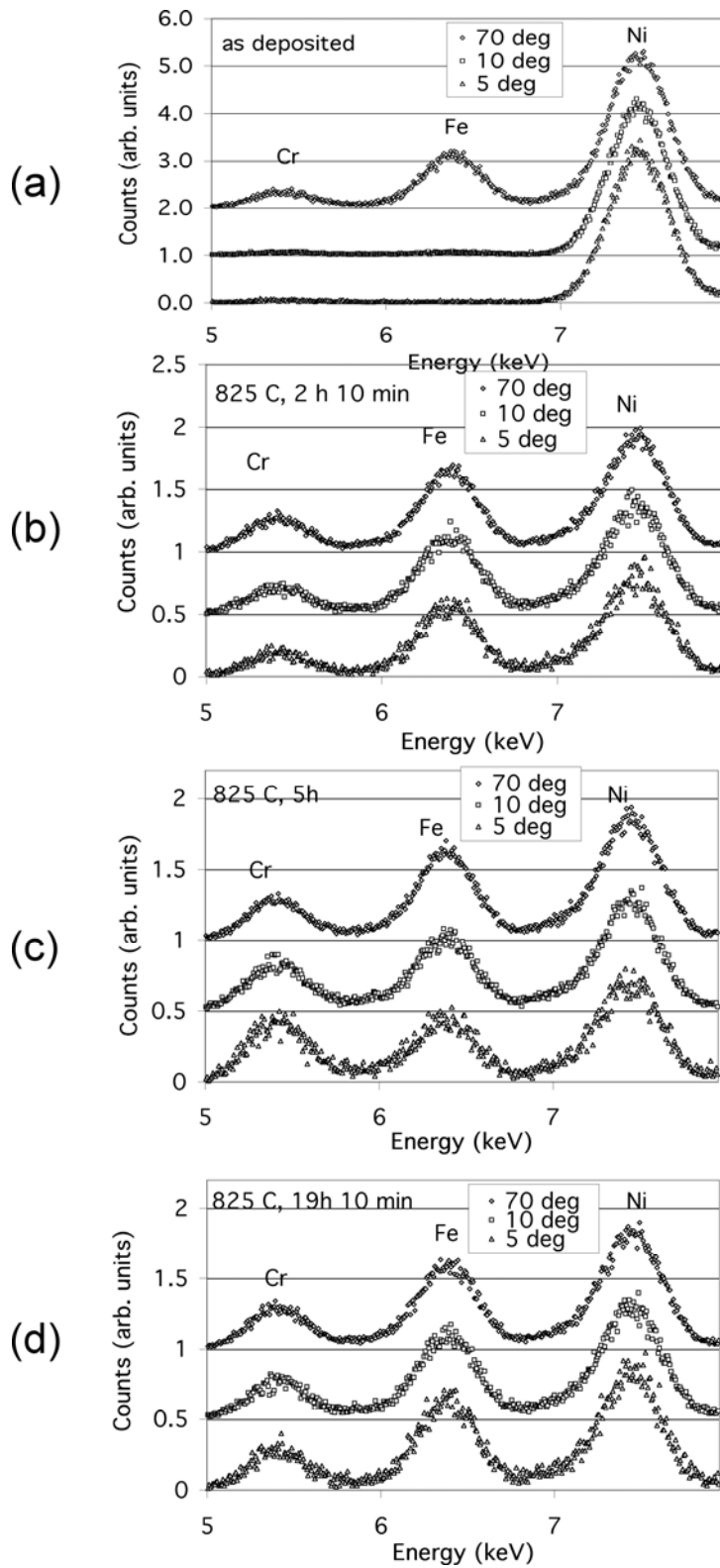
Fig. 10. Angular resolved XRF spectra for (a) an as-deposited Fe-Ni-Cr sample, and after annealing at 825°C for (b) 2 h 10 min, (c) 5 h, and (d) 19 h 10 min.

beneath the nickel. A simple analysis shows that the depth of the fluorescence signal is only ~0.07 μm for $2\theta = 5°$ and 0.14 μm for $2\theta = 10°$. Thus, only the nickel K_α peak is observed, since the top nickel layer extends to a depth of ~1.7 μm. For $2\theta = 70°$, the penetration depth increases enough that both chromium and iron peaks begin to emerge. In contrast, after 2 h 10 min, peaks from all three elements appear at each 2θ [Fig. 10(b)]. The homogeneity of the mixture then depends on the how the relative peak heights vary with 2θ. In Fig. 10(b), the ratio of the iron to nickel peak heights does not change from $2\theta = 5°$ to $70°$, but the ratio of chromium to nickel signal increases by 20% when 2θ changes from 5° to 10°. Thus, the sample surface is deficient in chromium, and local homogenization has not been achieved. No changes in the relative signal heights are observed after 19 h 10 min of annealing [Fig. 10(d)], indicating complete interdiffusion of the metals. The sample annealed 5 h [Fig. 10(c)] in the worst vacuum conditions produced a higher chromium peak at $2\theta = 5°$ than at 10° or 70°, suggesting preferential chromium segregation at the surface. This may be due to the formation of chromium oxide on the surface as the result of the poorer vacuum conditions.

Similar SEM and XRF analyses were performed on samples prepared at different temperatures and annealing times. It was found that annealing below 800°C frequently led to film delamination and that annealing above 900°C gave rise to unacceptable evaporation of chromium. In general, the best specimens were produced in the temperature range 850 to 875°C at an annealing time of ~5 h. In an attempt to reduce oxidation during annealing, we also performed interdiffusion by using encapsulation of the sample in quartz tubes backfilled with high-purity argon or forming gas and by pressing two specimen surfaces together. However, neither technique produced significant improvements. Both for the encapsulated and unencapsulated specimens, AES ion sputtering depth profiling showed that the sample surface after annealing in high vacuum had an oxide surface layer with a thickness of no more than a few nanometers. We speculate, therefore, that significant oxygen contamination does not occur during the annealing step.

The structural and chemical quality of the ternary alloy libraries was examined with scanning XRD. Phase diagrams determined from the results after annealing for 5 h and 3 h 20 min at 875°C, and after 2 h 10 min at 825°C are shown in Fig. 11(a–c). Calculated ternary alloy phase diagrams at 875°C and 700°C are shown in Figs. 12(a) and 12(b), respectively. The calculations were performed using the PANDAT^{TM} software package [23] and SSOL2—SGTE Solutions Database [24,25]. The phase diagrams measured for the experimental libraries are in reasonably good agreement with the expected behavior, with all the relevant phases appearing and their locations on the diagram being approximately correct. There are, however, a few notable differences. At compositions near the Ni-Cr binary side of the diagram, the measured libraries give the correct location of the γ (fcc) and α + γ (bcc + fcc) phases, but the extent of the α (bcc) phase is displaced to higher nickel concentrations than what is predicted by the calculated diagram [see Fig. 12(a)]. For compositions near the Fe-Ni binaries, the extent of α (bcc) phase is also greater than expected.

The most complex region in the ternary diagram [see Fig. 12(a)] is located between the iron and chromium corners at chromium concentrations from 20 to 70 at. % and iron concentrations from 25 to 65 at. % due to the appearance of the tetragonal intermetallic σ phase. In this region, four different phase fields are expected based on the calculated 875°C diagram: σ (tetragonal intermetallic) and a combination of σ with α, γ, and the α + γ phases. The positions and sizes of these phase fields are not reproduced well from library to library [Fig. 11(a and b)], and they deviate from the calculated diagram. The insufficient annealing time used for the library in Fig. 11(c) leads to the complete absence of the single-phase σ region in the diagram. However, the other regions in the phase diagram are reproduced well for this annealing condition. We suggest, therefore, that σ phase formation is relatively slow compared with the other phases.
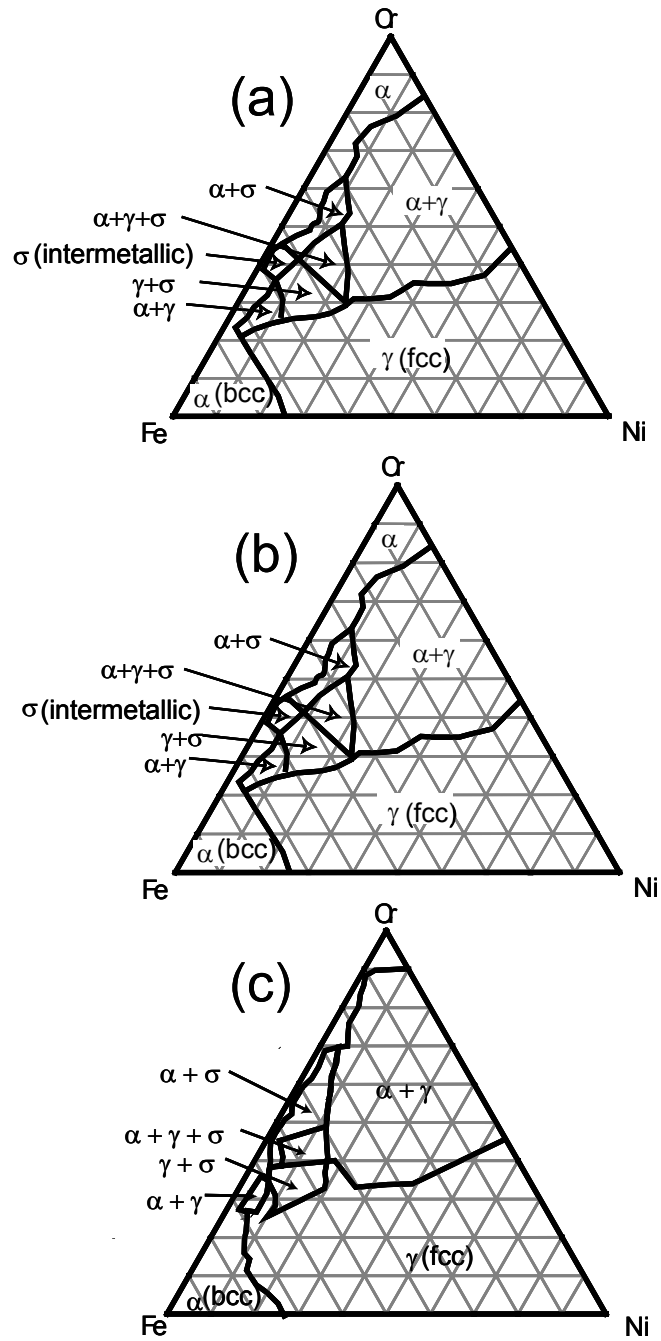
Fig. 11. Ternary phase diagrams measured after annealing at 875°C for (a) 5 h and (b) 3 h 20 min, and at 825°C for 2 h 10 min (c).
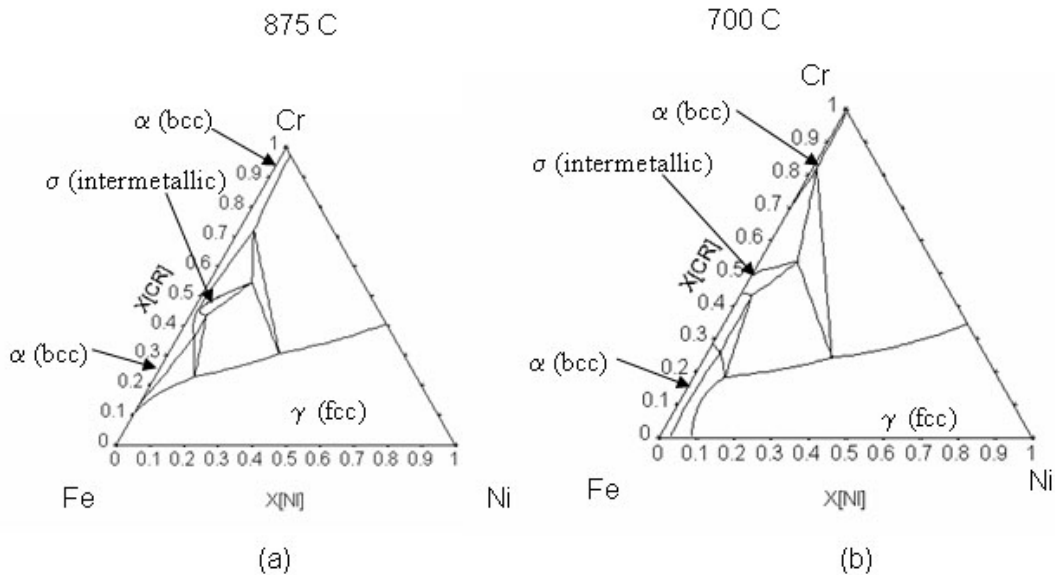
Fig. 12. Calculated ternary phase diagrams at (a) 875°C and (b) 700°C.

Many sources of error may contribute to the shifts in the observed phase locations. One is the lateral extent of the phase on the diagram and whether it is large enough to be experimentally measured by the XRD techniques. For example, the width of the σ phase in the library must be ~1–2 mm [Fig. 12(a)] so that it is comparable to the lateral resolution of the XRD measurements. This resolution could be improved at the cost of longer experimental time. Another problem results from changes in equilibrium during sample cooling. In this regard, it is instructive to compare the calculated ternary diagram at 875°C [Fig. 12(a)] to that at 700°C [Fig. 12(b)]. Inspection shows that the phase field boundaries in problematic locations are indeed different. For example, the phase change from fcc to bcc may occur during the cooling period in the iron-rich corner. Thus, the slow rate of cooling used during the experiments probably limits our ability to recreate true equilibrium conditions. This problem may be rectified by increasing the cooling rate. Impurities and the influences of the substrate on film orientation and epitaxy are other possible sources of difficulty.

In summary, this work shows that Ni-Fe-Cr alloy libraries of high quality can be prepared by depositing layers of Cr, Fe, and Ni on Al_2O_3 substrates followed by 2–5 h of interdiffusion at 825–875°C in high vacuum. The libraries incorporate all possible ternary compositions and compare generally well with the known ternary phase equilibria.

4.3 Preparation of Alloy Libraries by Co-deposition during Magnetron Sputtering

This section describes the techniques developed for preparing ternary thin film libraries by co-deposition from three physically separated but simultaneously operated magnetron sputtering sources. A spread in composition in the films was produced naturally due to the varying distance from the sputtering sources to different points on the substrate. The advantage of this technique is that alloying occurs automatically during film deposition, so there is no need for post-deposition annealing of the films. The technique also allows one to explore a variety of non-equilibrium phases with unique structures and properties. For example, for the Fe-Ni-Cr system, a non-equilibrium phase based on the α-Mn structure is observed at compositions close to $Cr_{17.5}Fe_{82.5}$. The unit cell of this unusual phase has a distorted bcc structure with 58 atoms [26,27]. The disadvantage of the technique is that only a

19

portion of the ternary composition space can be examined in one specimen due to geometric constraints on the deposition process.

To determine the extent to which Fe-Ni-Cr alloys made by co-deposition can be produced and to examine their structural stability at elevated temperatures, combinatorial libraries were deposited, annealed, and characterized using synchrotron XRD to examine the evolution of grain size and phase distribution.

Thin alloy films were grown on polished circular Al_2O_3 (sapphire) substrates, 102 mm in diameter with a $(1\bar{1}02)$ orientation. Substrates with a (0001) orientation were avoided, since they were found to produce a strong preferred orientation in the film [28]. The films were deposited onto fixed substrates using simultaneous RF magnetron sputtering from 51-mm-diam Cr, Fe, and Ni sources. The sputtering geometry is shown in Fig. 13. Each source was surrounded by a 51-mm-tall cylindrical shield to minimize cross-contamination. The target centers were 16.5 cm from the substrate center and were tilted at 32° relative to the substrate normal. The iron and nickel sources were 180° apart, with the chromium source 90° from both the iron and the nickel.

The pressure in the chamber base was 9×10^{-5} Pa, and the deposition pressure was 1.3 Pa argon. While sputtering conditions such as temperature, pressure, and deposition rate have a significant effect on the as-deposited film properties, the primary goal of this study was to investigate the phase evolution and stability of the Fe-Cr-Ni films as a function of annealing temperature. Consequently, a sputtering pressure was used that yields an optimum deposition rate for the system. The sputtering power was 160 W for iron and 60 W for chromium and nickel. The deposition time was 3 h, yielding a film thickness of ~2 μm. Incidental heating from the sources

Fig. 13. Three-source sputter deposition system.

raised the sample temperature to ~100°C during deposition. After deposition, the samples were annealed without breaking vacuum at 200, 400, 600, and 800°C, each for 2 h. An as-deposited sample was also studied.

The composition and structure were measured concurrently by XRF and XRD using synchrotron radiation at beamline X33-BM at the APS. The focused beam size of 1.0×0.25 mm^2 created a 1.0×1.0 mm^2 footprint on the sample when incident at a 15° glancing angle. The sample was rastered in a square grid in 2-mm steps. Data was collected for 2 s at each point.

Fluorescence spectra were acquired with a silicon drift detector (165 eV resolution at 6.4 keV). The detector views the sample at a 15° glancing angle. The integrated counts in the Cr, Fe, and Ni K emission lines were measured by least-squares fitting to Gaussian line shapes. The composition at each point was calculated from the ratio of these intensities [28]. Because the sample thickness is not constant, the thick-film limit was used in calculating the composition. This introduces a negligible error, since the X-rays are incident and fluorescence is measured at a glancing angle.

Diffraction patterns were acquired with a 1024 × 1024 CCD detector. Instrumental resolution was determined by the broadening of diffraction rings produced by the beam size; increasing the distance from sample to detector improved the resolution at the price of observing a smaller range of 2θ and a smaller section of each diffraction ring. Diffraction patterns were integrated to give 2θ scans, from which the phases were identified. Assignment of diffraction peaks is illustrated in Fig. 14. The peak width was measured by least-squares fitting to Pearson-7 line shapes. Peak breadth beyond instrumental resolution was generally caused by one of two factors: (1) microstrain, in which
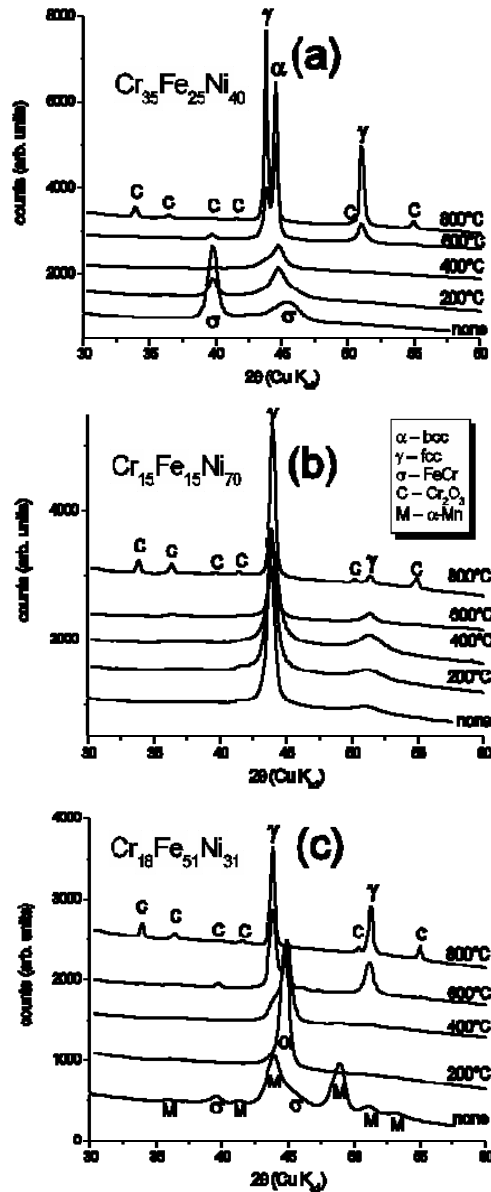
Fig. 14. Characteristic 2θ scans for samples annealed 2 h at indicated temperatures. "None" indicates the as-deposited film. Intensities are offset for clarity. 2θ values have been converted to the equivalent values for Cu $K_{\alpha 1}$ radiation for convenience.

21

distribution plane spacing, d, produces breadth $\Delta 2\theta = 2\tan\theta \,\Delta d / d$; and (2) particle or grain size, L, which produces line breadth $\Delta 2\theta = 0.94\lambda / (L\cos\theta)$ [29]. Due to the effects of texture, overlapping peaks, and the low scattering intensity from nanocrystalline materials, it is not possible to comprehensively determine the nature of the observed peak broadening, but the as-deposited fcc phase gives clear (111) and (200) reflections. The ratio of the widths of these reflections is consistent with grain-size broadening, indicating that grain size rather than strain makes the dominant contribution to peak width [29]. The average grain size at each composition was determined from the Scherrer equation [30]. Because the films grow with a strong preferred orientation, only one peak of each phase could be used in the grain size analysis: bcc (110), fcc (111), σ-FeCr (002), and α-Mn (332). Instrumental resolution was measured using a microcrystalline tungsten sample and was subtracted from the peak widths. Grain sizes greater than ~30 nm could not be reliably measured due to limited instrumental resolution.

As shown in Fig. 14, qualitative trends can be seen in 2θ scans for three characteristic compositions annealed at four temperatures. Peaks are broad for the as-deposited samples, and sharpen on annealing. A dramatic phase evolution occurs: a single-phase σ-FeCr film [$Cr_{35}Fe_{25}Ni_{40}$, Fig. 14(a)] converts to bcc at 200°C, and to mainly fcc at 800°C, while a single-phase fcc film [$Cr_{15}Fe_{15}Ni_{70}$, Fig. 14(b)] remains so, and a mainly α-Mn film [$Cr_{18}Fe_{51}Ni_{31}$, Fig. 14(c)] converts to bcc at 200°C and fcc at 600°C. Peaks for Cr_2O_3 are visible at 600°C and 800°C; this is most likely a result of residual gas in the annealing vacuum [31].

Ternary plots of grain size evolution are shown in Figs. 15–18. The lighter black lines in each plot denote the edge of the film, spanning a roughly triangular region of the ternary section. Note that the

Fig. 15. Grain size and phase fields for σ-FeCr structure. Hatching indicates compositions where the σ–FeCr phase is not observed.

Fig. 16. Grain size and phase fields for the fcc structure. Hatching indicates compositions where the fcc phase is not observed.

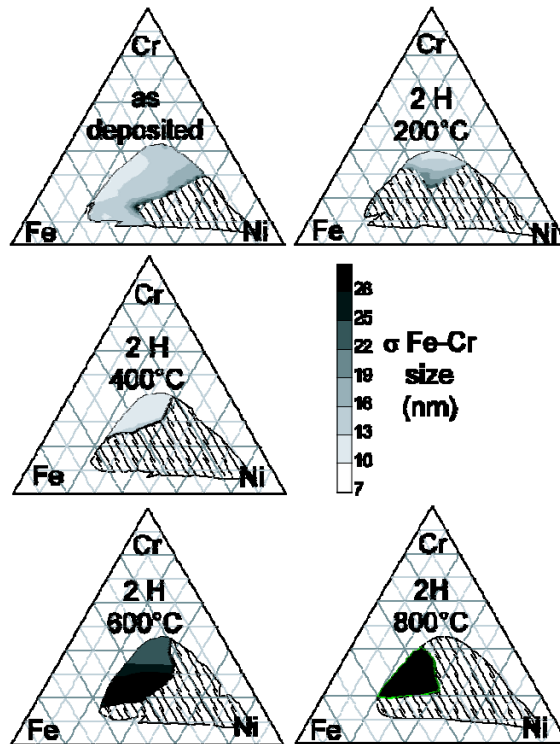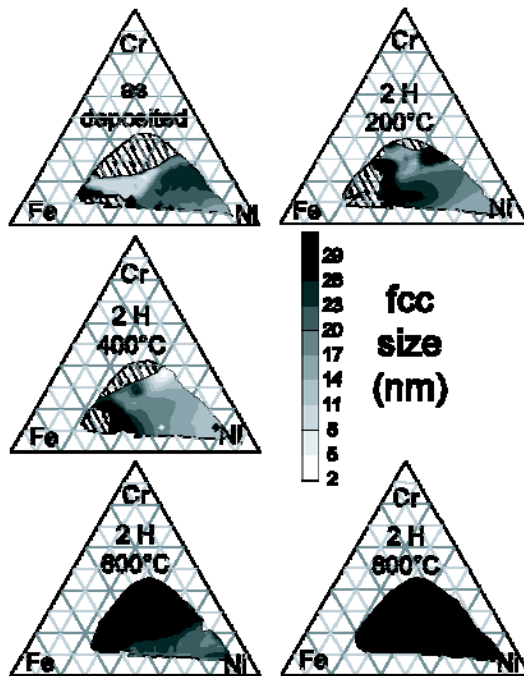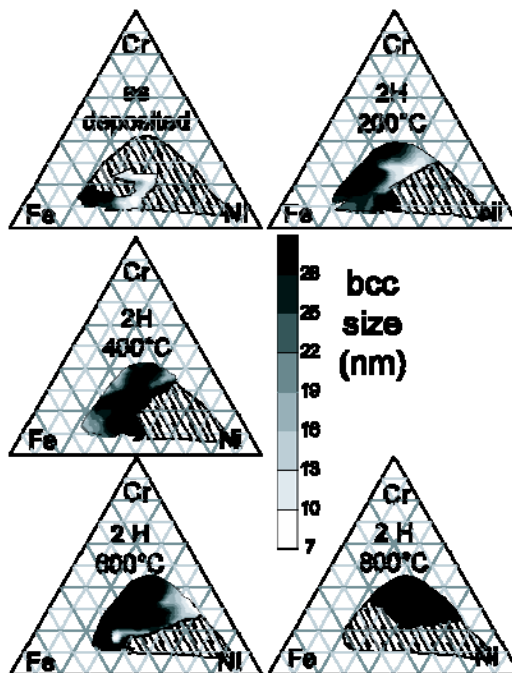**Fig. 17. Grain size and phase fields for the bcc structure.** Hatching indicates compositions where the bcc phase is not observed.

range of composition achieved in the specimens covers only about one-quarter of the ternary composition space. This is the primary limitation of the ternary co-deposition technique. Also note that each sample spans a slightly different composition due to temporal variations in sputter source output. Although not explored here, other compositions that allow one to cover more of the ternary diagram can be achieved by varying the geometric arrangement of the sample and sputtering targets.

The σ-FeCr structure occurs over a wide range of compositions in the as-deposited film (Fig. 15). Annealing at even the lowest temperature (200°C) contracts the phase field greatly, probably because σ-FeCr is metastable at low temperatures. The as-deposited grain size of 10–13 nm does not increase significantly until 600°C, where significant grain growth (>30 nm) occurs.

The fcc structure, on the other hand, spans a phase field less than its equilibrium extent below 600°C; at this temperature and above, it spans the entire film (Fig. 16). The as-deposited fcc-structure film has a grain size than depends strongly on composition: 5-nm nanocrystalline crystallites occur in the iron-rich region where fcc, bcc, and σ-Fe structures coexist, while 20-nm crystallites form in the nickel-rich, single-phase fcc field. As for σ-FeCr, significant grain growth occurs at 600°C.

The bcc structure appears largely as a transitional phase (Fig. 17). It occurs over a narrow compositional range in the as-deposited film, is found over a much wider range at intermediate temperatures (200–600°C) as σ-FeCr transforms to bcc, and becomes less widespread at the highest temperature (800°C) as bcc transforms to fcc. The as-deposited grain size distribution is again bimodal, with 12-nm crystallites in the four-phase coexistence field and larger crystallites in the iron-rich bcc + σ-FeCr field.

Fig. 18. Grain size and phase fields for α-Mn structure. While observable at 200°C and 400°C, the α-Mn peaks are very weak. Hatching indicates compositions where the α-Mn phase is not observed.

The α-Mn structure occurs in significant quantity only in the as-deposited sample (Fig. 18). The structure is barely detectable in the annealed samples [Fig. 14(c)], so the significance of the phase field and grain size in the sample is uncertain. The grain size is 5–10 nm as-grown (Fig. 18).

As the samples were annealed at progressively higher temperatures, the phase content evolved from largely σ-FeCr, first to more bcc, and finally to mainly fcc. The phase fields at 800°C are essentially those of the equilibrium diagrams presented earlier (Fig. 12); differences of <5% may be caused by the formation of Cr_2O_3, which leads to a difference between the composition measured by XRF and the actual composition of the metal. The samples annealed at lower temperatures are clearly not in equilibrium. The as-deposited 200°C and 400°C samples contain four-phase fields, in violation of the Gibbs phase rule [32]. The phase field for the 600°C sample is far from the equilibrium (Fig. 12). The time and temperature required for equilibration (2 h at 800°C) is consistent with the observations of alloys prepared by discrete layer deposition followed by annealing Cr-Fe-Ni films.

For some compositions and phases, grain growth was not observed at all. In the iron-rich region, for example, the σ-FeCr and fcc phases transform to bcc at the lowest annealing temperature of 200°C.

24

The small quantities of the α-Mn phase which remain after annealing at 200°C and 400°C cannot be considered as representative of the material: most of it has transformed to bcc as well. For the other compositions and phases, grain growth occurs too abruptly for a meaningful analysis of growth rate. Increased grain size for σ-FeCr, for example, was measured at a single temperature of 600°C; at 800°C the grain size was too large to measure due to limited instrumental resolution. Growth rates and activation energies could conceivably be measured by these techniques for a reduced number of compositions. With a data collection time of 3 s for each composition, an in situ annealing study could measure a diffraction pattern from each of 200 compositions every 10 min.

In conclusion, the co-deposition technique produces a variety of non-equilibrium phases that evolve toward equilibrium when annealed at high temperatures. In addition, there are significant changes in the initially nanometer grain sizes as the specimens are annealed. The co-deposition method of alloy library preparation thus allows one to explore a variety of the equilibrium and non-equilibrium phases and structures and their stability. The primary disadvantage of the technique is the limited range of ternary composition that can be achieved.

4.4 Preparation of Alloy Libraries by Electron Beam Melting

The studies of alloy library preparation by thin film deposition and electron beam melting were limited to the binary alloy system Ni-Cr. However, the techniques can easily be applied to ternary and higher alloy systems by depositing multiple thin films on the substrate. Electron beam (EB) melting is an entirely new combinatorial design technique that can produce alloys similar to industrial cast alloys. The methods do not use high-temperature diffusion for alloying and produce alloys that are in a non-equilibrium state similar to that of cast alloys. The methods take far less time to produce a sample than is required by diffusion.

As shown in Fig. 19, the alloy libraries were made by vapor-depositing thin-wedged films of metal A on a substrate of metal B, and then alloying by localized melting with a focused EB welding (EBW) system. The EB welds run the length of the wedge to create a compositional gradient. The EBW technique creates melted and solidified alloys similar to those produced by conventional casting methods. The composition and mechanical properties of the specimens were assessed using EDS and nanoindentation.
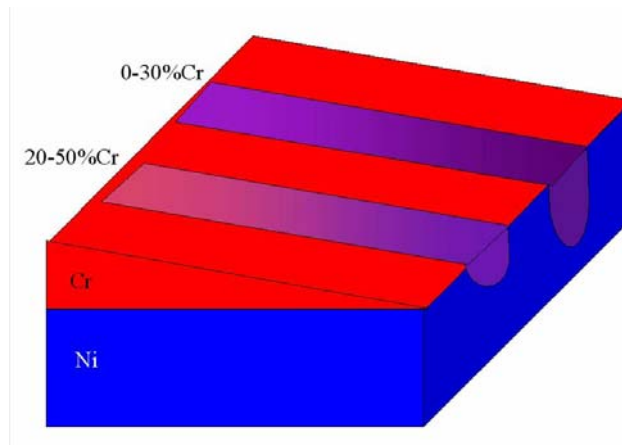
Fig. 19. Schematic of a combinatorial sample prepared by EBW showing several compositional ranges.

As noted above, EBW techniques can produce materials in a very short time. After a substrate is polished, it takes only about a day to deposit the necessary wedged film and only a few hours to make several EB welds across the length of the sample. By contrast, it can sometimes take months to establish suitable diffusion between bulk samples in order to create the necessary alloy library [8, 33–34]. To date, most techniques for producing combinatorial alloy libraries have been based on diffusion multiples that give equilibrium structures. Alloys produced in industry are frequently not in the equilibrium state. Therefore, there are distinct advantages to samples made by welding.

A high-vacuum physical vapor deposition system (PVD) was used to prepare the alloy library specimens. Electron-beam heating was used to evaporate high-purity nickel or chromium, and a film was deposited onto a substrate of the other metal. The deposition system incorporated a movable shutter placed in the line of sight between the targets and the substrate. Translating the shutter parallel to the substrate as the target was vaporized caused a wedge-shaped film of element A to be deposited onto substrate B.

After film deposition, a precision, fully automated EBW system was used to alloy the films by local EB melting. The beam can produce melting up to several millimeters in depth, and the diameter of the molten zone can be constrained to less than 1 mm, thus minimizing lateral spreading of the alloying components. After alloying of the component species is accomplished, a specimen that is pure A at one end and pure B at the other is produced, with compositions varying systematically in between, corresponding to the entire binary composition range. By controlling the scanning speed and the EB power, the heating and cooling rates can be varied, and their effects on film microstructure can be investigated.

As shown schematically in Fig. 19, several compositional ranges can be produced on the same sample because the melt depth can be varied up to several millimeters by controlling the EB power. This provides an additional degree of freedom in the alloy compositions, since controlling the melt depth can vary the amount of the substrate material incorporated into the alloy. For example, one weld may have a concentration gradient ranging from 0 to 30 at. % Cr, while another weld with higher EBW power settings may have a gradient ranging from 20 to 50 at. % Cr.

It was initially hoped that one weld of a chromium film on a nickel substrate would establish the full compositional spectrum. However, the compositional ranges along the length of the weld only covered ranges of 30%, and a maximum chromium concentration of 70 at. % was achieved. Thicker chromium films were deposited in an attempt to overcome this obstacle, but there were limitations related to evaporation, crucible size, and deposition rate measurements. Moreover, when thicker films were deposited, they were unsuccessful because of poor adherence between the film and the substrate. Therefore, an EBW of nickel films deposited on chromium substrates was used to achieve the chromium-rich ranges of the alloy system.

To prepare the nickel substrates, a small batch of 99.99% pure nickel was melted and cast into a mold with dimensions of $1 \times 0.5 \times 6$ in. This casting was warm-rolled at 400ºC to a thickness of 0.125 in. and then cold-rolled to 0.060 in. The finished nickel strip was ~1 in. wide. The strip was then cut into 1.5-in. sections and mounted in epoxy with the 1×1.5 in. face down. Likewise, a small batch of 99.99% pure chromium was melted and cast into a similar mold to prepare the chromium substrates. Chromium is difficult to roll, so the casting was cut into 1×1.25 in. sections with a thickness of 0.15 in. These sections were also mounted in epoxy with the large face down.

The mounts were hand-polished to maintain uniform polishing thickness through P600 grit, and then polished using a Struers automated polisher with 6-, 3-, and 1-mm diamond suspensions. The mounted substrates were then soaked in methylene chloride overnight to dissolve the epoxy and

release the substrates. Ethanol was used to clean the substrates and remove any excess epoxy or methylene chloride. The final thickness of the nickel substrates was ~0.058 in., and the final thickness of the chromium substrates was ~0.12 in. The substrates were cleaned in acetone and then ethanol in an ultrasonic bath for 5 min each.

A CVC, Inc. (now Veeco), PVD chamber was used to deposit films. The system used a Telemark-271 EB gun to heat the source material for vaporization. The samples were inverted directly above the source material and were attached to a mounting stage. A movable shutter directly below the mounting stage moved continuously during deposition to create a wedged film on the substrate.

After the chamber had reached a vacuum of less than 1.0×10^{-7} torr, the heater lamp near the stage was turned on and the lamp power was increased to 20 V and 6 A. The samples were heated for ~90 min to raise the temperature of the substrates to ~90ºC. This higher temperature aided in the adhesion of the metal vapor to the substrates. The appropriate density and z-ratio (acoustic impedance ratio) of the source metal was programmed into the computer controlling the crystal microbalance to provide accurate measurements. The density and z-ratio of nickel are 8.91 g/cm^3 and 0.331, and the density and z-ratio of chromium are 7.20 g/cm^3 and 0.305, respectively.

The movable shutter was set to open 1.5 in. and close over 120 s with no dwell time. The accelerating potential for the EB source was slowly increased to 10 kV at a rate of 1 kV every 10 s. The current was increased slowly until the crystal microbalance began to detect some deposition. The beam position and amplitude were adjusted to optimize the deposition rate, while an effort was made to maintain a rate of 12–16 Å/s for chromium and a rate of 3–6 Å/s for nickel.

Chromium has a faster deposition rate than nickel due to its higher vapor pressure. The deposition rate of chromium could be increased beyond 16 Å/s, but it was kept lower to increase adherence to the substrate and to establish a more uniform wedged film. For chromium films, it was best to use a lower-amplitude setting and move the electron beam across the chromium pellet source often to maintain a uniform deposition rate. Due to its high vapor pressure, the chromium would sublime into a vapor state without melting first. For nickel films, it was best to use a higher-amplitude setting that covered most of the cast nickel source. High current was needed to first melt a large pool on the source, allowing a large area of molten nickel to then vaporize.

A Leybold-Heraeus electron beam welder was used to create the welds that alloyed the nickel with the chromium. The samples were loaded such that the direction of the wedge ran parallel to the x-direction of the welder. This simplified the later process of programming the welding direction. The samples were clamped down tightly to ensure that any welder vibrations would not move the samples or create wavy weld lines.

The welder was not used until the vacuum had reached a pressure of less than 3.2×10^{-4} torr. Several EBW parameters were found to greatly affect the characteristics of the weld. As expected, increases in current and accelerating potential increased the depth of the weld, with the accelerating potential having the greatest affect. The travel speed of the weld played a factor in the surface characteristics of the weld, which could have a great affect on the nanoindentation results. The weld with the faster travel speed has a wavelike appearance with non-uniform edges, and the surface appears very rough. The weld with the slower travel speed appears much smoother and more uniform. Higher accelerating potentials also caused the welds to be rougher.

The EBW accelerating potentials that created a suitable weld were between 100 and 130 kV, although several welds were also created at potentials of 150 kV with faster travel speeds. The current

depended on the potential used; the best welds were created when the power (current x-potential) was near 100 W. The better welds used a travel speed of 10 ipm.

All chromium concentrations of samples and cast standards were measured in atomic percentages. Standards of pure nickel and chromium were arc-melted in a water-chilled copper mold, as were 15 Ni-Cr alloys with chromium concentrations (at. %) of 20, 30, 40–95 in multiples of 5, and 98. The chromium and nickel starting materials were greater than 99.995% purity. The pure metals were carefully weighed and then mixed by arc melting, with the buttons flipped and remelted five times to ensure good mixing. Total weight loss after melting and casting was less than 0.2%, which led to negligible changes in alloy composition after melting. The standards were cross-sectioned, mounted in epoxy, and polished through a 1-mm diamond suspension. The standards were examined by optical microscopy, SEM, EDS, and nanoindentation; and these data were used to compare all of the welded combinatorial samples.

Though SEM cannot be used to determine crystal structure and orientation, it was used to visually identify phases within the welded sample. The backscattered electron (BSE) detector was used to enhance the contrast between the phases of the binary system. The magnification capabilities of SEM also enabled visualization of grain boundaries, voids, microsegregation, and the interaction between the deposited film and the weld pool.

The elemental compositions were determined by EDS in conjunction with SEM. This provided composition details for the small regions of secondary phases, as well as covering large regions such as the weld surface. The EDS instrument is computer interfaced and uses software that provides a quantitative measurement showing the composition of each element within the combinatorial array with a standard deviation of less than 3% [35].

A Hitachi S4100 SEM was used along with a Gresham Sirius EDS detector. To produce high quality images, we often used lower voltages to minimize charging. Most commonly the accelerating voltage was 5–10 kV, the condenser lens was set at 11 pA, and the stage distance was 15 mm. To excite all chromium and nickel peaks, the accelerating voltage was increased to 20 kV, the condenser lens was reduced to 9 pA, and the stage distance was increased to 20 mm.

The analysis software for the EDS system was Revolution from 4pi Analysis, Inc. Revolution uses ZAF corrections based on the relation

$$\frac{C}{C_{sd}} = \frac{I}{I_{sd}} \frac{F}{F_{sd}} \ ,$$

(2)

where C is concentration, I is X-ray line intensity, and F is the ZAF matrix correction. The subscript sd refers to the same quantities for the standard element in use for the analysis. If standardless analysis is used, a mathematical model for the standard is substituted [35].

Nanoindentation was used in conjunction with the chemical and structural characterizations to investigate the fundamental mechanical properties of the combinatorial specimens. The goal was to correlate mechanical properties with chemical composition and microstructure. There is a great deal of experience in this area at ORNL, and several fully automated, state-of-the-art nanoindentation systems were available for use. The two mechanical properties that can be most easily probed are elastic modulus and hardness [36], both of which can be measured with spatial resolutions greater than 1 μm. The nanoindenter was set up to make a series of indentations at specified locations on the alloy library surface and automatically collect and store all the data needed to obtain hardness and

modulus as a function of position on the combinatorial sample surface. Approximately 50 to 100 indentations could be made during an overnight run, depending upon the setup parameters. Thus, mechanical properties could be obtained for a fairly wide range of chemical compositions in a relatively short time.

An MTS Nanoindenter II with a Berkovich indenter was used for all mechanical property measurements. The continuous stiffness mode was used with a frequency of 45 Hz. The surface search distance was 9000 nm, and the maximum drift rate prior to tests was 0.1 nm/s. The loading rate was 0.05 nm/s, and the unloading rate was 300 nm/s. Indents were made to a maximum depth of 1000–1200 nm for weld surface tests, and to a maximum depth of 400–600 nm for weld cross-section tests. Indents were made to a maximum depth of 200-400 nm for all polished cast standards.

For the combinatorial samples, surface indents were positioned down the centerline in an array from one end of the weld to the other with indentation spacing around 800–1000 nm. Most positions were set up in an array, although some indentations had to be individually positioned to avoid the surface cracks, especially in the welds with higher chromium concentrations. Indentations on the cross sections of the weld were individually positioned to ensure that they were within the alloyed region.

Poisson ratios of 0.31 and 0.21 were used for the nickel and chromium standards, respectively. A Poisson ratio of 0.25 was used for all other alloy standards and for all welded samples. Results were obtained from data taken at depths of 800 nm for all indentations taken from the weld surface and of 400 nm for all indentations taken from the weld cross sections. Results of the cast standards were measured from the data taken at a depth of 200 nm. The accuracy of the Nano II modulus data is usually expected to be within 10% of the literature values. The data for the combinatorial EB welds were compared with the data from the cast standards to validate the precision of the EB weld hardness and modulus.

Results will be discussed for Ni-Cr standards, samples made with chromium films on nickel substrates, and samples made with nickel films on chromium substrates. The results from the welded samples are compared with the results from the alloy standards to determine if the combinatorial welds have properties similar to those of cast structures.

Cross sections of the Ni-Cr cast standards were made to examine the microstructure at different compositions. Two-phase microstructures were not observed in the cast standards of 20, 30, or 40 at. % Cr, but were seen in the standards of higher chromium concentrations. Fig. 20 shows a micrograph of the Ni-30Cr cast standard, which shows evidence of microsegregation within the solid solution. Fig. 21 shows a micrograph of the Ni-70Cr cast standard, where the light regions are the chromium-rich α-phase, and the dark regions are the nickel-rich γ-phase. The casting shows a dendritic structure, with the dendritic direction toward the center of the cast button, as expected. More cracking and voids appeared in the standards as the chromium concentration increased because of the large solidification temperature range.

The standards were tested by nanoindentation to evaluate the mechanical properties of hardness and modulus. The surfaces were polished through 1 μm diamond suspension prior to testing. The polishing reduced the data scatter and yielded results with low deviation. For the standards with one phase, indentations were made in a regular 3 × 4 pattern to obtain enough data to determine uniformity. For the standards within the binary phase region, several indentations were made individually on the γ-phases and the α-phases, and were also made in a regular 3 × 4 pattern to examine both phases and regions near phase boundaries. More indentations were made in the Ni-70Cr
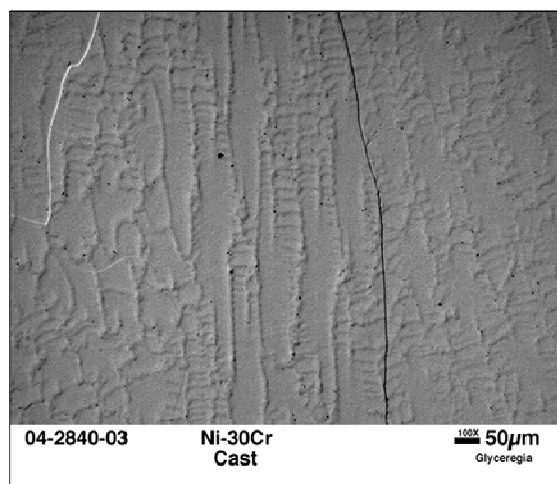
Fig. 20. Optical image of the Ni-30Cr cast standard.
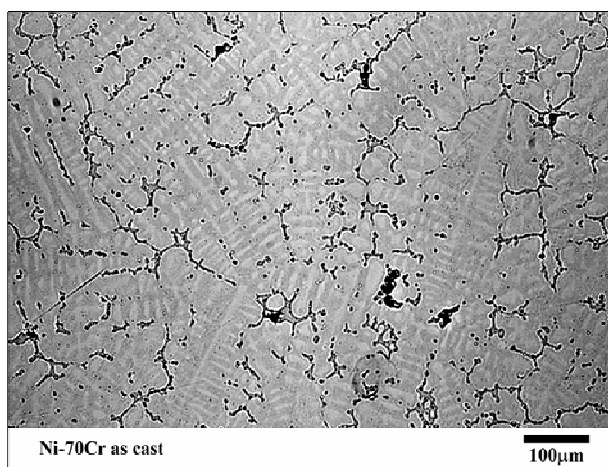
Fig. 21. Optical image of the Ni-70Cr cast standard.

cast standards to ensure that both phases were sampled to obtain the full hardness spectrum of the phases.

As shown in the Ni-Cr phase diagram in Fig. 22, there are three regions of interest: the nickel-rich solid solution (γ-phase), the chromium-rich solid solution (α-phase), and a dual-phase region. The elastic modulus of alloys is strongly dependent upon elemental composition, while other characteristics such as phases, heat treatments, or surface conditions exert a negligible influence [37]. For the sake of discussion, it is useful to compare the measured moduli to those predicted by a simple linear rule of mixing. In this case, the modulus should show a linear tendency between the modulus of pure nickel (200 GPa) and the modulus of pure chromium (279 GPa) [37]. Hardness, on the other hand, is dependent on many factors besides just alloy composition. Phase distribution, grain size, and surface conditions can have a great effect on the measured hardness of the alloy. Therefore, a linear "law of mixing" is not necessarily useful, except in single-phase regions where solid solution strengthening may be important.

Figure 23 shows the nanoindentation elastic modulus results for the Ni-Cr alloy standards. The modulus of the pure nickel standard averaged 194.7 GPa, and the modulus of the pure chromium standard averaged 277.1 GPa. Both of these values are very similar to the literature values of 200 and 279 GPa, respectively. The law-of-mixing line shown in the figure represents the linear expectancy of the modulus between 200 and 279 GPa.

The data points for the Ni-Cr cast alloys were all within the general trending of the law of mixing, although there were several points for the higher-chromium alloys that were higher than expected. The standards up to 40 at. % Cr all had data points within 10% of the law-of-mixing line, but the standards of 50 and 56.14 at. % Cr had several modulus measurements that fell as much as 17% below the law-of-mixing line. The cast standards of 70 and 85 at. % Cr were on the other end of the spectrum, with some of the modulus measurements more than 30% higher than the law-of-mixing line.

It should be noted that although the modulus should be primarily dependent on the total composition, the indentations were so small that they often hit parts of or all of only one phase within the alloy. This explains the scatter in the two-phase regions. Assuming the 900ºC isotherm of the Ni-Cr phase

30
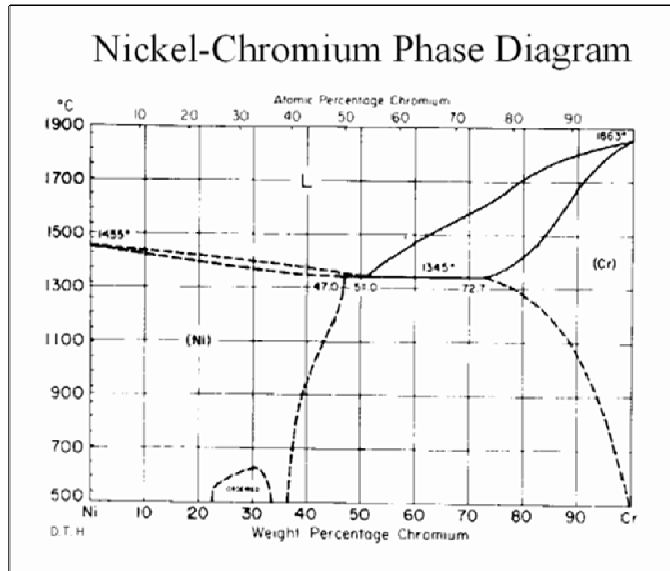
Fig. 22. Ni-Cr phase diagram [38].
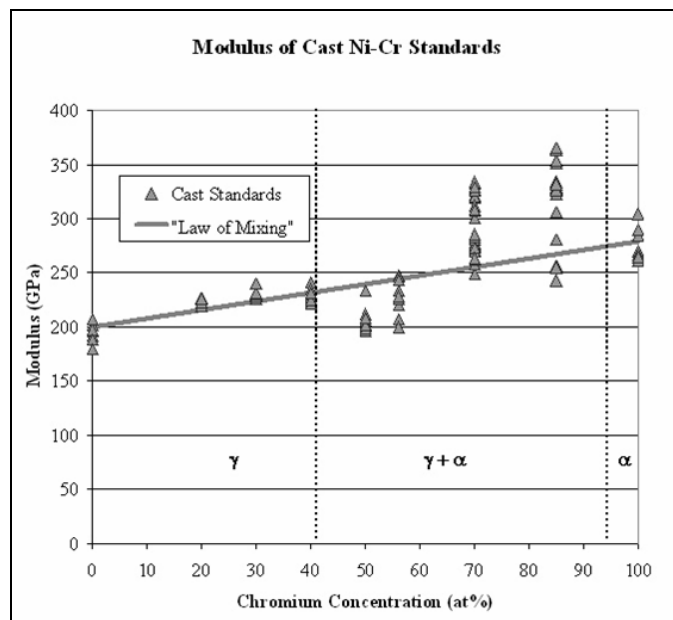
Fig. 23. Modulus of cast Ni-Cr standards.

diagram, the saturated γ-phase should have a chromium concentration near 40 at. %, and the saturated α-phase should have a chromium concentration near 95 at. %. This would cause the individual phases to have moduli varying between ~232 and 275 GPa, respectively. The actual scatter in the data is somewhat greater.

The hardness values for the cast Ni-Cr alloy standards are shown in Fig. 24. The hardness values up to 40 at. % Cr show very little deviation and an upward tendency with a generally constant slope. This is consistent with the expectations of the single-phase region as it reaches its solid solution solubility limit. The hardness of pure nickel was ~1.2 GPa, and the hardness of the Ni-40Cr alloy was ~3.1 GPa. In the cast alloys of less than 40 at. % Cr, no dual phases were observed. At 50 at. % Cr

31

Fig. 24. Hardness of cast Ni-Cr standards.

the hardness values begin to increase at a much steeper slope and the scatter becomes greater. The hardness values for the Ni-70Cr and Ni-85Cr standards extend from 7 and 8 GPa to nearly 13 GPa. The hardness of the γ-phase at the solubility limit is in the range of 3 to 4 GPa. However, alloys with greater than 54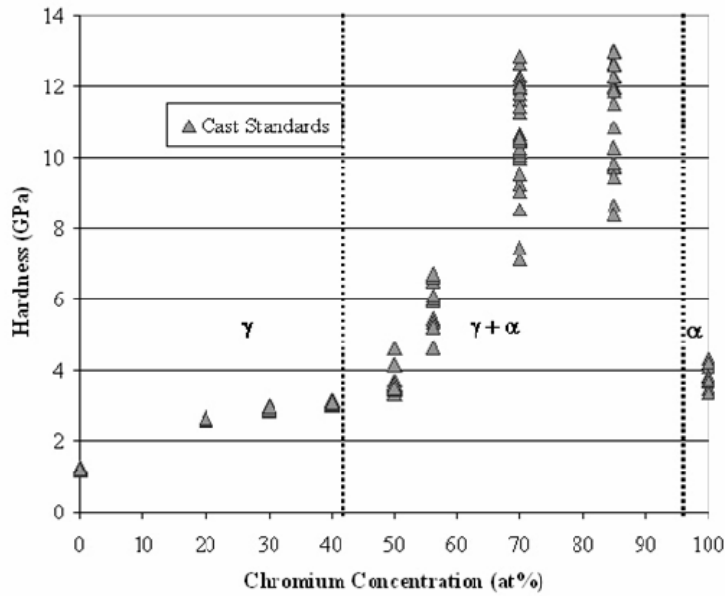 at. % Cr will have α-phase regions and γ/α eutectic regions. Therefore it is difficult to isolate the γ-phase for nanoindentation because it is finely intermixed in a eutectic.

The large deviation is primarily due to the binary phase region that occurs above 50 at. % Cr, although it was also observed that the alloys with higher chromium concentrations had a higher tendency for cracks and voids. These cracks and voids were also visible in the cast pure chromium, which explains why the scatter of hardness for chromium was so much higher than for nickel. The hardness of pure chromium was ~3.8 GPa.

The hardness values obtained by nanoindentation were verified by Vickers microhardness tests. Figure 25 shows the hardness results obtained from the VH200 microhardness tests using a load of 200 g. These results show tendencies similar to those for the nanoindentation data. The absolute hardness values are not directly compared due to differences in the definitions of Vickers and Berkovich hardness, as well as differences in loads used to make the measurements.

The chromium films deposited on nickel substrates adhered well, and alloy libraries were made very easily compared to the samples of nickel films on chromium substrates. Figure 26 shows a BSE image of a cross section taken at the thick end of the film. The EBW parameters were a potential of 130 kV, a current of 0.8 mA, and a travel speed of 10 ipm. The chromium film can be seen on both sides of the weld, and the weld pool can be distinguished from the nickel substrate. Chromium has a much higher melting point than nickel (1875ºC and 1453ºC, respectively) [12], which can explain why the weld pool begins slightly under the still-intact chromium film. At the surface of the weld pool near the edges are darker regions within the lighter weld pool. These darker regions are either

32

Fig. 25. Vickers microhardness of cast Ni-Cr standards.
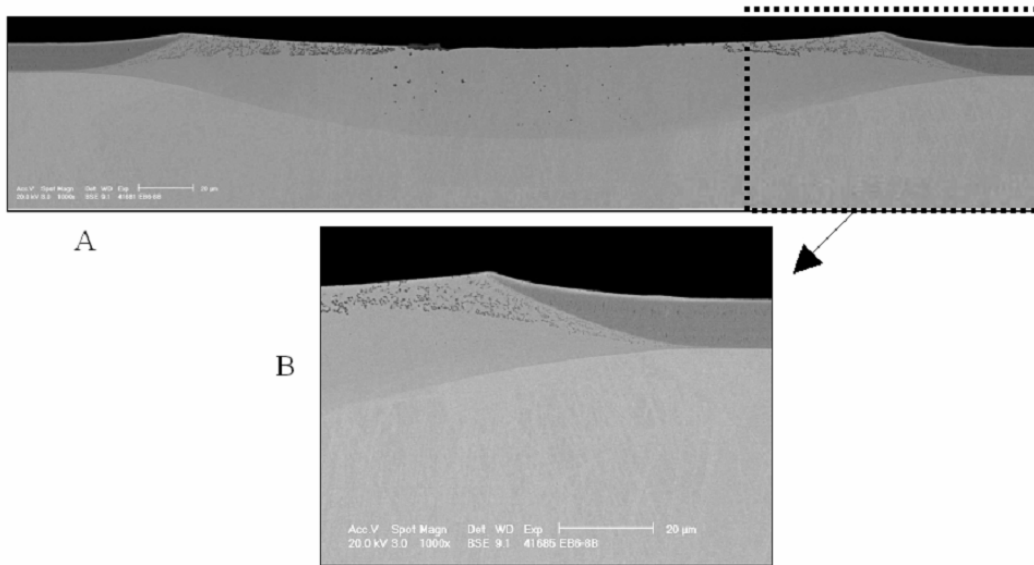
Fig. 26. BSE images of a weld cross section: (a) full weld pool and (b) edge of same weld at higher resolution (concentration of ~44 at. % Cr).

unmelted pieces of the chromium film or regions of α-phase, but there was not enough evidence to reach a definitive conclusion. The surface of this weld was examined by EDS and determined to have a chromium concentration of 44 at. %, which is around the concentration where the α-phase may reside in the γ-phase matrix.
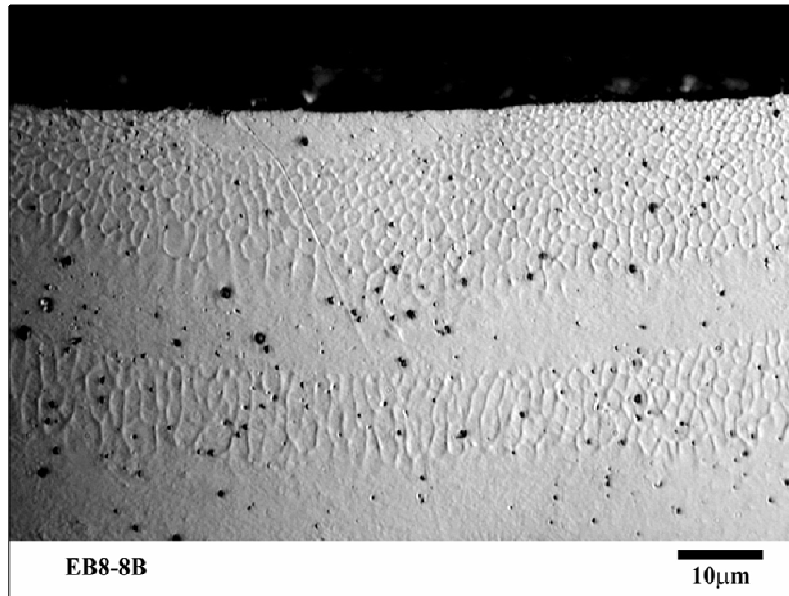
Fig. 27. Cross section of EB weld (130 kV, 0.7 mA, 10 ipm) (concentration of ~10 at. % Cr).

Figure 27 shows another cross-sectional images taken with an optical microscope after the sample was etched with glyceregia to reveal the microstructure. The EBW parameters were a potential of 130 kV, a current of 0.7 mA, and a travel speed of 10 ipm. The image shows several lines in the welds that were caused by the movement of the electron beam. The small black spots are voids within the weld that were caused by shrinkage during solidification.

The concentration change along the length of the weld showed a linear tendency, as expected. An example of the concentration gradient is shown in Fig. 28. As described above, the full composition range was not obtained, and these three welds had ranges only from 18 to 50 at. % Cr. The significant increase in scatter in the data at the thick end of the wedge at concentrations greater than 40 at. % Cr could be caused by the rougher surface of the weld or by the introduction of a secondary phase. There could also be regions of unmelted chromium film at the thick ends of the wedged film.

Though the surface details appeared to show strong tendencies that indicated a true combinatorial alloy library, several tests were performed to verify that these alloys were uniform throughout the weld. First, cross sections were made, and the welds were examined by EDS to evaluate the depth of the chromium concentration. Figure 29 shows the concentration profile of a typical EB weld. The top of the cross section had a concentration that was only 2 at. % lower than the concentration evaluated from the surface of the weld, indicating that the EDS examinations from the surface were accurate. The concentration held fairly constant at 26–28 at. % Cr to a depth of ~18 mm, which is half of the total weld depth of 37 mm. The weld still had above 20 at. % Cr at a depth of 28 mm, and the chromium concentration dropped to 10 at. % at the weld pool boundary.

Indentations were made on the polished cross-sections to prove that the indentations made on the rough surface would agree with more reproducible data. Cross sections were made at the ends of a sample, and three welds were examined. Four or five indents were made in each cross-sectional weld, and the hardness values obtained were compared with the hardness results taken from the surface. Figure 30 shows the results of the hardness of the cross-sections at each end (squares) compared with the hardness from the surface (diamonds). The inset shows images of the indentations taken in the
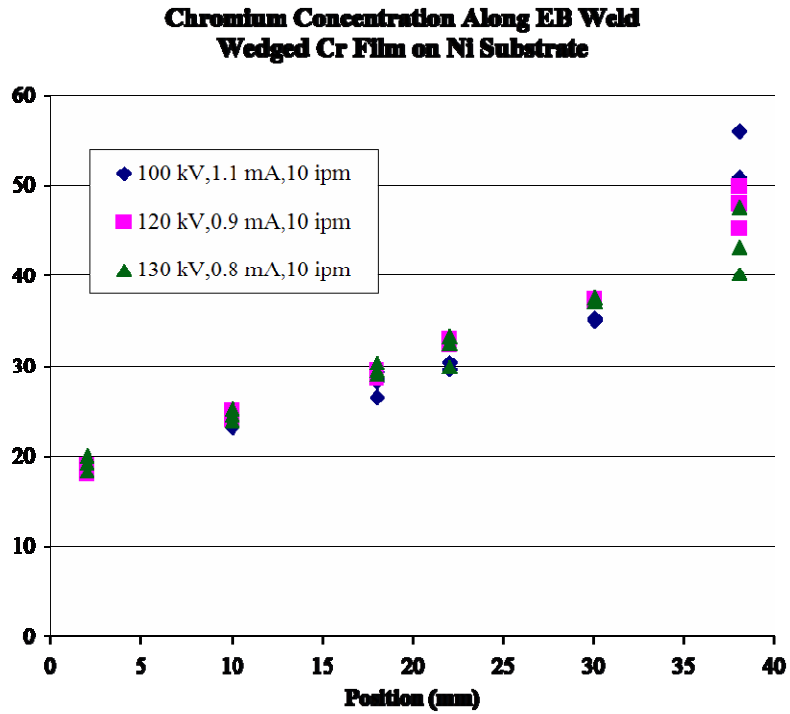
34

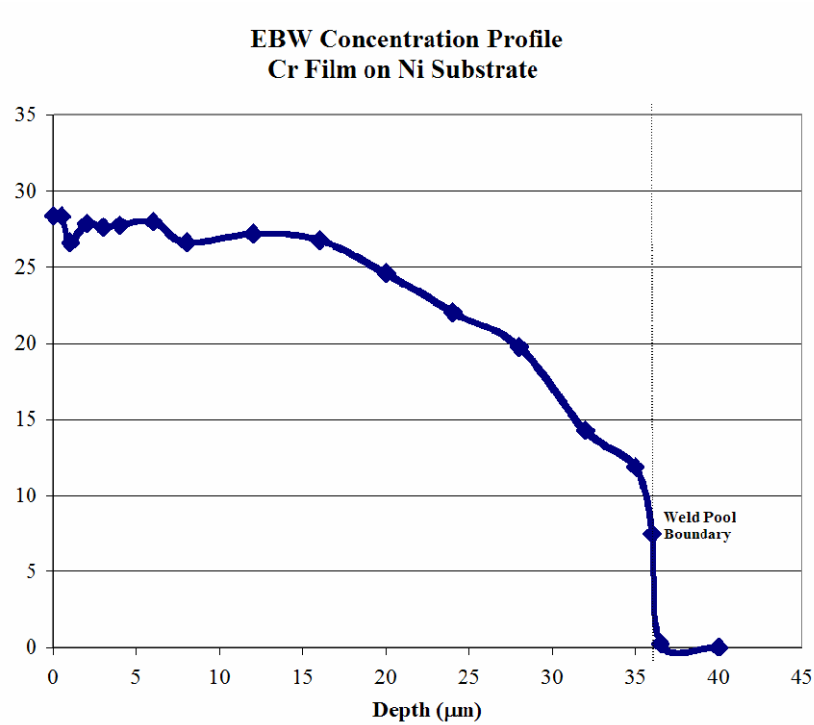**Fig. 28. Concentration gradient along length of weld for chromium films on nickel substrates.**

Fig. 29. Concentration profile through the depth of EB weld; chromium film on nickel substrate.
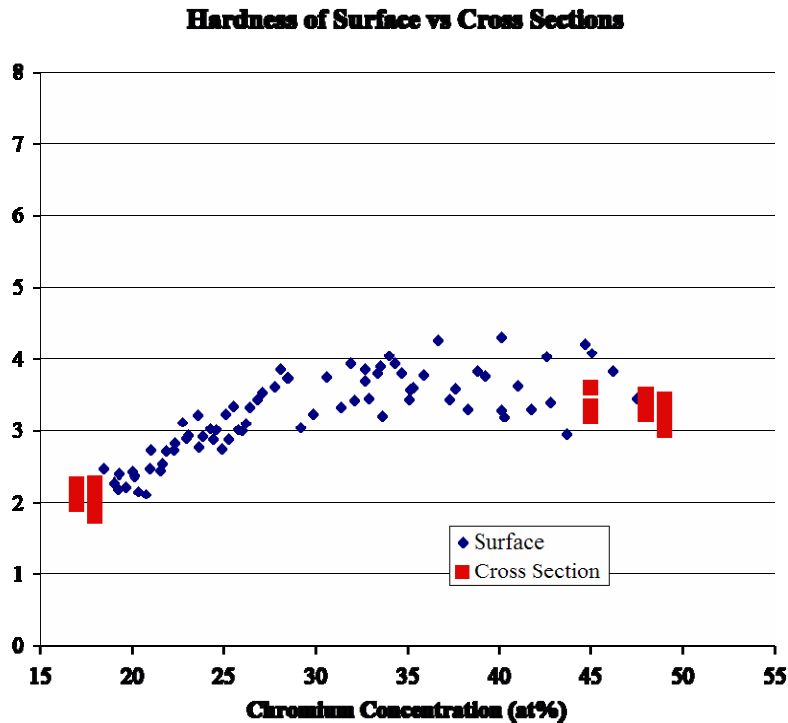
Hardness of Surface vs Cross Sections

**Fig. 30. Hardness values for indentations taken at surface compared
with those taken from polished cross sections at either end.**

cross-section of the weld pool. The hardness results from the surface compared well with the results from the polished cross-section, showing that the results from the surface adequately represent the true hardness of the weld. This also showed that the surface roughness did not have a significant effect on the results obtained by nanoindentation.

Another test was conducted to determine the effect of the surface roughness on the results obtained by nanoindentation. Three different welds with rough surfaces were evaluated by nanoindentation, and then the surfaces were hand-polished with P4000-grit silicon paper to reduce the extremely rough surface. Nanoindentation was again performed at the same regions of these three welds, and these hardness results are compared with the original hardness results in Fig. 31. The diamonds indicate measurements made from the rough surface, and the squares indicate measurements made from the polished surface of the cross section. It can be seen that polishing the surface did little to reduce the scatter of hardness data obtained from the three welds.

These results indicate that most of the data scatter cannot be attributed to surface roughness. Another possible contributing factor to the scatter could be voids within the weld caused by the rapid cooling of the weld pool before the material completely settles from the turbulence of the welding process. The existence of two discrete phases could explain scatter in regions greater than 40 at. % Cr.

Two samples of nickel films on chromium substrates were examined, using EBW parameters similar to those for the samples with nickel substrates. For one sample an accelerating potential of 100 kV was used, and for the other sample, an accelerating potential of 120 kV. A constant travel speed of 10 ipm was used for both samples, and only the current of the EB weld was varied to create the different
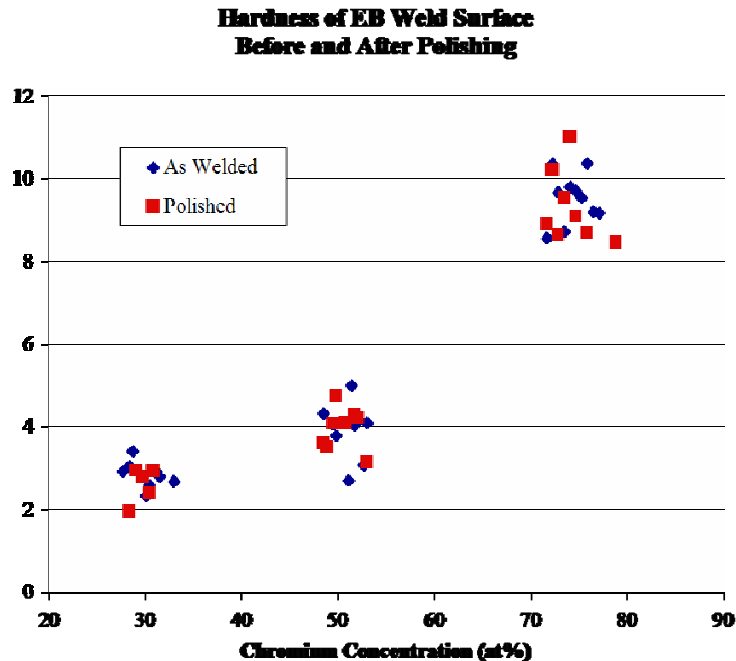
Fig. 31. Hardness of EB weld surface before and after polishing.

compositional ranges. The nickel films did not adhere well to the chromium substrates, especially at the end of the wedge where the thickness was greatest, and large cracks were visible on the surface of almost all of the welds made on the chromium substrates.

It was again observed that the welds produced with the higher currents were deeper than those produced with the lower currents, and the deeper welds had a higher chromium concentration. The glyceregia attacked these welded samples much more rapidly than the samples with chromium films on nickel substrates, and the voids in the welds were very apparent. The SEM images in Fig. 32 show a weld on a chromium substrate; the two phases are more easily distinguished in the image on the right. The dark regions are the chromium-rich α-phase, and the light regions are the nickel-rich γ-phase. The two phases are apparent throughout the weld, from the surface to the bottom of the weld pool.

Many of the tests to verify the uniformity of the samples with nickel substrates could not be used for the samples with chromium substrates because of the presence of dual phases. As can be seen in Fig. 32, the welds created on the chromium substrates had finely intermixed regions of γ-phases and α-phases, each with distinctly different properties. As with the samples with the nickel substrates, cross sections of the welds were examined by EDS to evaluate the concentration profile, shown in Fig. 33. The top of the cross section had a concentration that was only 5 at. % lower than that evaluated on the surface of the weld, indicating that the EDS examinations from the surface were reasonable. However, the concentration did not vary smoothly through the depth of the weld due to the separation of the two phases.

Combining all the samples, both those with chromium films on nickel substrates and those with nickel films on chromium substrates, the EB welds were able to produce a combinatorial alloy range of 1 to 95 at. % Cr. There were only a few gaps in the composition range that were not covered, and it
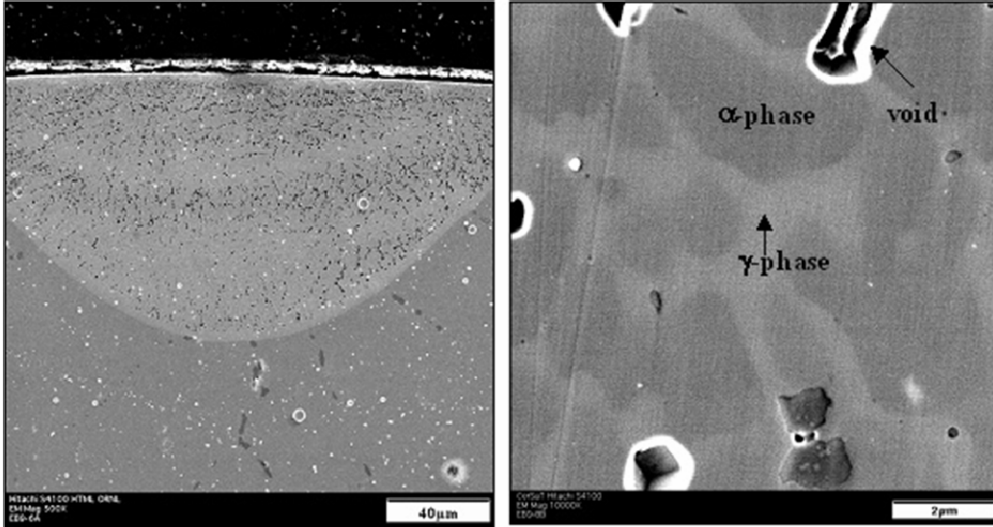
Fig. 32. SEM images of cross sections of EB welds (concentration of ~65 at. % Cr).
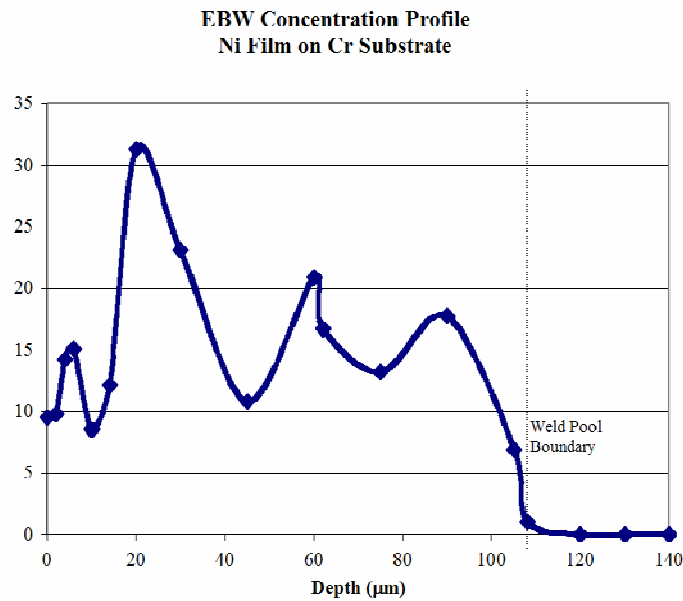
Fig. 33. Concentration profile through depth of EB weld (nickel film on chromium substrate).

was much more difficult to produce a complete compositional gradient on the samples with the chromium substrates. The combined results for the modulus of the Ni-Cr combinatorial alloys are shown in Fig. 34. The results coincide with the law-of-mixing line until almost 40 at. % Cr, and then the modulus values are lower than the law of mixing for chromium concentrations of 40–80 at. %.

The hardness values for all of the Ni-Cr combinatorial alloys are shown in Fig. 35, along with an insert of the Ni-Cr phase diagram. The hardness results generally coincide well with the hardness of the cast Ni-Cr standards. As with the cast standards, the hardness of the combinatorial welds increased linearly from 1.2 to 3.5 GPa with little deviation from 0 to 40 at. % Cr. From 40 to 50 at. %

38

Fig. 34. Modulus of all combinatorial EB welds.

Fig. 35. Hardness of all combinatorial EB welds.

Cr the hardness remained steady at ~3.5 GPa, and then greatly increased to values between 6 and 13 GPa from 70 to 85 at. % Cr. This high hardness is attributed to the chromium-rich α-phase, and the large scatter at this composition is due to the difference in hardness between the γ-phase and α-phase in this dual-phase region.

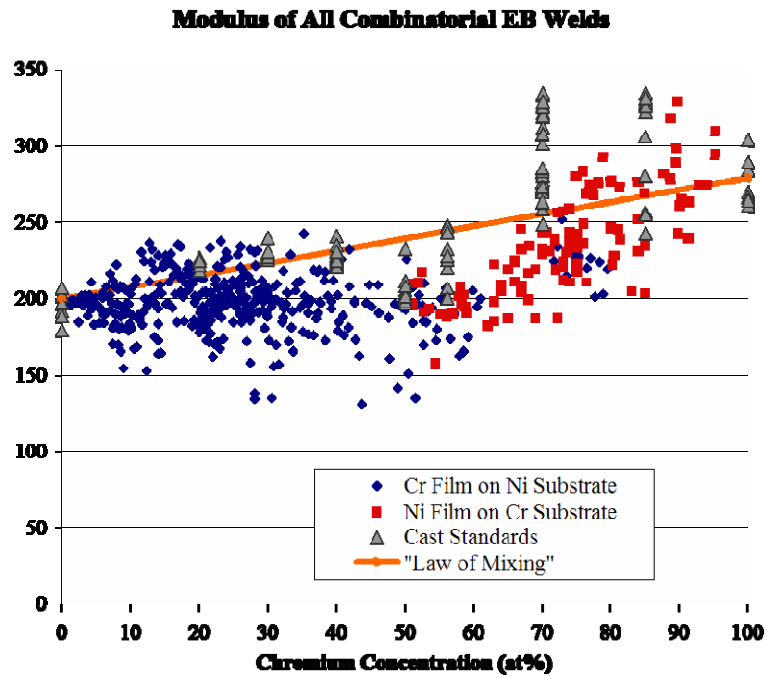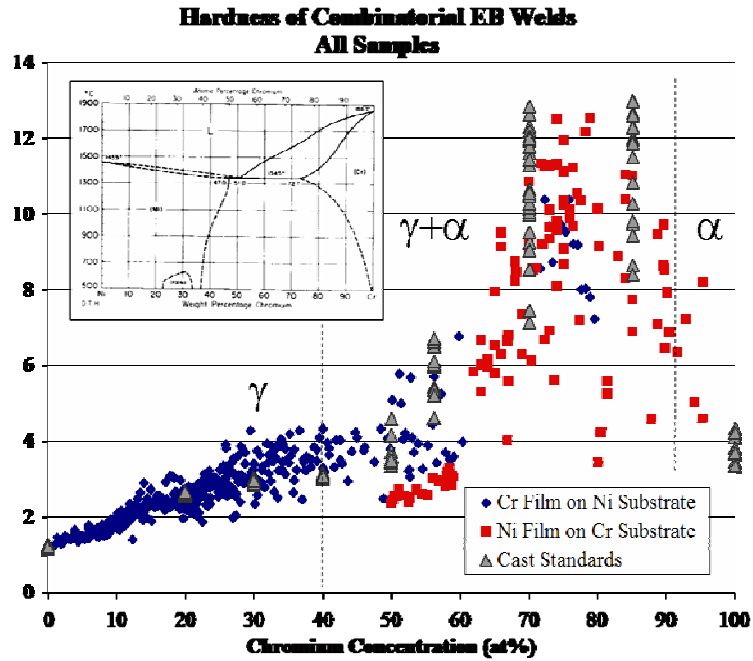It was difficult to obtain results with greater than 85 at. % Cr, and the compositional range above 95 at. % Cr was not achieved at all. Thus, there is no clear understanding of trends greater than 85 at. % Cr and no specific evidence to what happens at the solution saturation point of the α-phase. Of the few data points acquired in this region, all fall below a hardness value of 9 GPa. Since the saturated α-phase is assumed to have the highest hardness values measured (nearly 13 GPa), it is assumed that the saturation point of the α-phase is between 80 and 90 at. % Cr, a range in which only a few hardness values reached 11 GPa. Although there is not enough data to make a conclusive argument, it appears that hardness values begin to decrease after ~85 at. % Cr toward the hardness value of pure chromium, which was ~3.8 GPa.

In conclusion, the combinatorial method of vapor-deposited films alloyed with bulk substrates by EBW worked extremely well for the Ni-Cr binary alloy system. There was a linear gradient of composition along the length of the welds that could be easily measured from the surface. The mechanical properties of hardness and modulus obtained by nanoindentation could also easily be characterized from the surface of the rough welds. Both the mechanical and compositional measurements were representative of the measurements taken from the more polished and uniform cross sections and were comparable to cast standards. The cross sections of the EB welds showed segregation and phase transformation comparable to those exhibited by the cast Ni-Cr standards. The compositions of the alloyed weld pools remained relatively constant through at least half the weld depth, which was more than 30 times the depth of the nanoindentation taken from the surface.

The modulus measurements showed no strong tendencies, and the scattering of modulus results limited any conclusive correlations about various composition changes. However, all of the modulus values were within reasonable deviation from the standards set by cast Ni-Cr alloys, though most fell below the linear law-of-mixing value. There were strong trends in the hardness measurements that followed similar tendencies of the standard Ni-Cr alloys prepared by melting and casting. The hardness values also showed trends that coincided with the composition changes associated with the Ni-Cr phase diagram. The hardness results obeyed a clear trend in the nickel-rich γ-phase, where the single-phase compositional range between 0 and 40 at. % produced only limited scatter in the data.

We conclude that producing combinatorial Ni-Cr alloy libraries by physical vapor deposition and EBW and then rapidly characterizing the chemical and mechanical properties with EDS and nanoindentation is a very useful screening method for rapid assessment for alloy design. One sample of a nickel substrate with a chromium wedged film and one sample of a chromium substrate with a nickel wedged film, with as few as two or three welds per sample, are sufficient to establish the entire composition range. These methods have proven successful for the combinatorial alloy design of Ni-Cr alloys, and they can easily be applied to other alloy systems.

4.5 Nanoindentation Mechanical Property Measurement in Ternary Alloys

As discussed in the previous section, nanoindentation proved a very useful tool for rapidly characterizing the mechanical properties of binary alloy libraries based on the Ni-Cr system. Studies were also undertaken to assess the utility of this technique in the characterization of ternary libraries. The libraries we examined were prepared by the vapor-deposition and annealing method. Some of the measurements proved difficult due to surface roughness, which produces scatter in the

nanoindentation data. In this instance, meaningful results could be obtained only by taking large numbers of measurements and applying statistical procedures to account for the scatter. In addition, the data sets were large and unwieldy, so algorithms had to be developed to automate the data reduction and graphical presentation.

We found that when a relative rather than an absolute property measurement is acceptable, measuring the contact stiffness by dynamic methods has distinct advantages. The absolute property parameter is directly related to the ratio of the elastic modulus to the hardness, and because of this, it has the advantage of being relatively insensitive to roughness (as well as substrate influences).

An example of the rapid assessment of mechanical properties by nanoindentation methods is given in Fig. 36, where hardness contours in a rectangular region of an Fe-Ni-Cr ternary library annealed for 5 h at 875°C (i.e., close to equilibrium) are plotted. The hardness data were obtained overnight using an automated procedure that sampled ~400 different locations evenly spaced in the region. The figure shows that the hardness rises dramatically in the vicinity of the σ phase, as would be expected based on its complex crystal structure. In this manner, nanoindentation can be used to rapidly identify composition regions of interest. Similar maps can be made of the elastic properties as characterized by the nanoindentation measurement of Young's modulus.
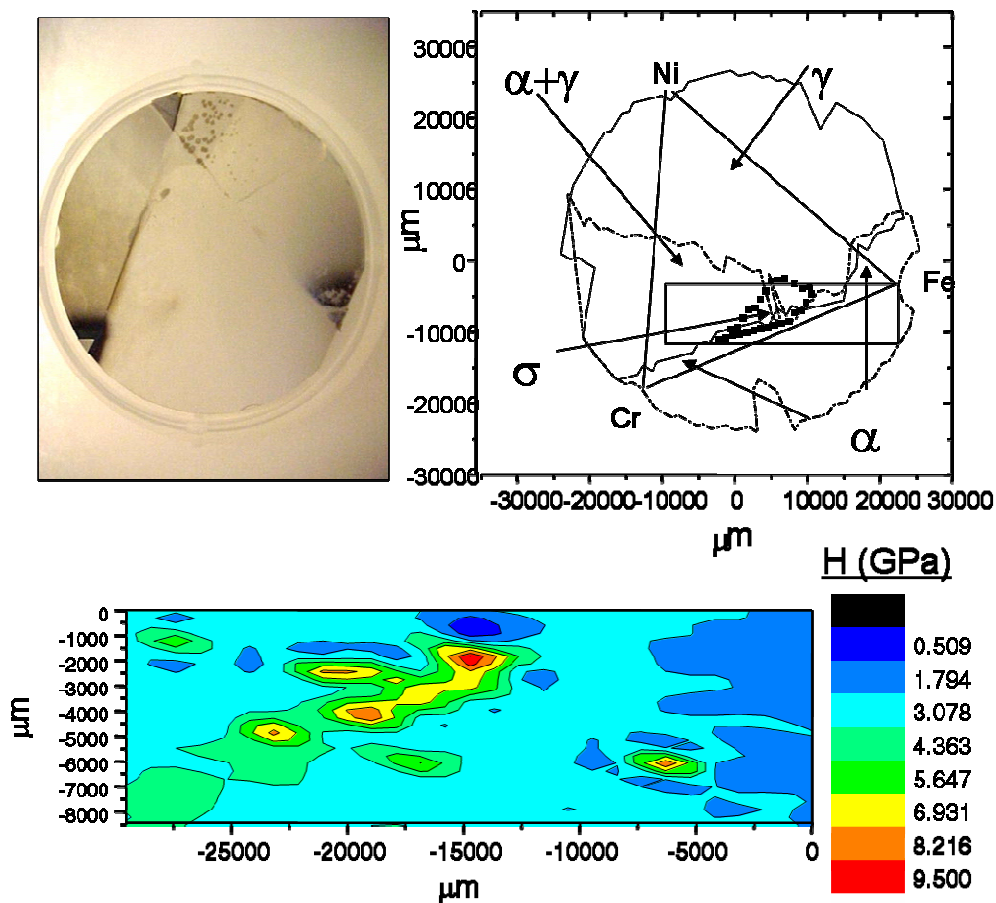

Fig. 36. Nanoindentation measurements of hardness contours in a rectangular region of an Fe-Ni-Cr ternary library annealed for 5 h at 875°C.

4.6 Corrosion Assessment

A simple technique for assessing corrosion resistance was developed by masking selected areas of the alloy library surface with a polymeric corrosion inhibitor laid down in a grid pattern. After subjecting the surface to a corrosive agent and removing the grid by dissolution in acetone, the extent of local corrosion was determined by profiling the depths of the steps in the surface where the corrosion had taken place relative to the adjacent uncorroded masked area.

The corrosion susceptibility of several Ni-Cr alloy libraries prepared by the EB melting technique was assessed by immersing them in 8 cc H_2O, 14 cc 35% HCl, and 18 cc 70% HNO_3, which is used to etch Ni-Cr alloys, and measuring the depth of material removal as a function of position (and, therefore, composition) with an ADE MicroXam optical profilometry system with depth resolution of ~1 nm. This procedure is very fast, since the optical profilometer provides fully quantified depth measurements over the entire field of view in a matter of seconds.

Typical results are shown in Fig. 37, where the depth of corrosion is plotted as a function of the local chromium concentration. Curiously, increasing the chromium content produced a greater susceptibility to corrosion for this corrosive agent. Used in this way, the technique provides a valuable rapid assessment tool for corrosion susceptibility.
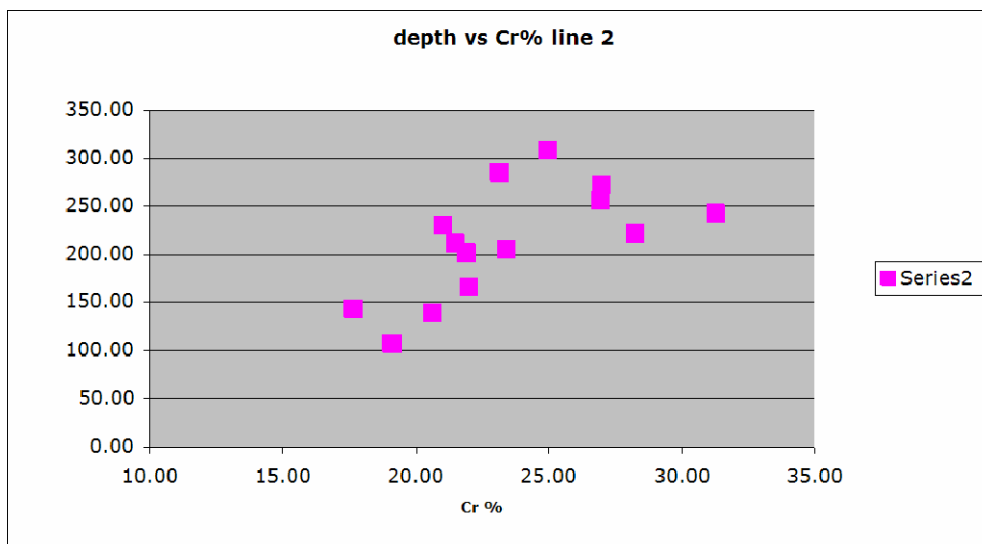
Fig. 37. Depth of corrosion as a function of local chromium concentration for a Ni-Cr binary alloy library prepared by the EB melting technique.

4.7 Carburization Assessment

Several thin film alloy libraries made by the thin film deposition and annealing technique were carburized by depositing a thin film of carbon on the surface and then annealing. Many of the films delaminated, but a few remained intact. These were taken to the APS for structural characterization by synchrotron techniques—specifically, XRD measurements of changes in lattice parameter, a standard figure of merit for carburization effectiveness. Unfortunately, the samples proved too rough to allow measurement of the lattice parameter with the precision needed to establish the degree of carburization.

As an alternative approach, libraries of Ni-Cr made by the EBW technique were carburized using standard gas carburization techniques by placing them in contact with graphite powder in a vacuum annealing furnace for 16 h at 875°C. They were subsequently examined by nanoindentation to correlate the degree of carburization with mechanical properties. Electron microprobe analysis was used to measure the carbon content at several points along the weld. Nanoindentation revealed an interesting result: the hardness and elastic modulus of most Ni-Cr compositions actually decrease following carburization. This behavior was later confirmed to occur in bulk as-cast specimens as well. A more detailed scientific study of the origin of this behavior is in order.

5. Publications and Presentations

5.1 Publications

E. D. Specht, A. Rar, G. M. Pharr, E. P. George, P. Zschack, H. Hong, and J. Ilavsky, "Rapid Structural and Chemical Characterization of Ternary Phase Diagrams Using Synchrotron Radiation," *Journal of Materials Research* **18,** 2522–2527 (2003).

E. D. Specht, P. D. Rack, A. Rar, G. M. Pharr, E. P. George, and H. Hong, "Nonequilibrium Structures in Codeposited Cr-Fe-Ni Films," in *Combinatorial and Artificial Intelligence Methods in Materials Science,* ed. R. A. Potyrailo, A. Karim, Q. Wang, and T. Chikyow, MRS Symp. Proc., Vol. 804, pp. JJ6.3.1–6 (2004).

A. Rar, E. D. Specht, H. M. Meyer III, M. L. Santella, E. P. George, and G. M. Pharr, "Preparation of Ternary Alloy Libraries by Means of Thick Film Deposition and Interdiffusion: Structure and Mechanical Properties," in *Combinatorial and Artificial Intelligence Methods in Materials Science,* ed. R. A. Potyrailo, A. Karim, Q. Wang, and T. Chikyow, MRS Symp. Proc., Vol. 804, pp. JJ9.2.1–6 (2004).

A. Rar, E. D. Specht, E. P. George, M. L. Santella, and G. M. Pharr, "Preparation of Ternary Alloy Libraries for High-Throughput Screening of Material Properties by Means of Thick Film Deposition and Interdiffusion: Benefits and Limitations," *Journal of Vacuum Science and Technology* A22, 1788–1792 (2004).

A. Rar, J. Frafjord, J. D. Fowlkes, E. D. Specht, P. D. Rack, M. L. Santella, E. P. George, and G. M. Pharr, "PVD Synthesis and High-Throughput Property Characterization of Ni-Fe-Cr Alloy Libraries," *Measurement Science and Technology* 16, 46–53 (2005).

E. D. Specht, P. D. Rack, A. Rar, G. M. Pharr, E. P. George, J. D. Fowlkes, H. Hong, and E. Karapetrova, "Metastable Phase Evolution and Grain Growth in Annealed Nanocrystalline Cr-Fe-Ni Films," *Thin Solid Films,* in press.

J. J. Frafjord, A. Rar, M. L Santella, E. P. George, and G. M. Pharr, "Combinatorial Design of Nickel-Chromium Alloys by Physical Vapor Deposition and Electron Beam Welding," in preparation for submission to *Journal of Materials Research*.

5.2 Presentations

A. Rar, E. D. Specht, E. P. George, and G. M. Pharr, "Preparation of Ternary Alloy Libraries for High-throughput Screening of Material Properties by Means of Thick Film deposition and Interdiffusion: Benefits and Limitations," Annual Meeting of the American Vacuum Society, Baltimore, MD, November 2003.

A. Rar, E. D. Specht, H. M. Meyer, E. P. George, and G. M. Pharr, "Preparation of Ternary Alloy Libraries by Means of Thick Film Deposition and Interdiffusion: Structure of the Resulting Layers," Fall Meeting of the Materials Research Society, Boston, MA, December 2003.

E. D. Specht, P. D. Rack, A. Rar, E. P. George, H. Hong, and G. M. Pharr, "Nonequilibrium Structures in Codeposited Cr-Fe-Ni Films," Fall Meeting of the Materials Research Society, Boston, MA, December 2003.

G. M. Pharr, E. P. George, and G. M. Pharr, "Development of Combinatorial Methods for Alloy Design and Optimization," ITP Portfolio Review Meeting, Crystal City, VA, June 2004.

G. M. Pharr, E. P. George, M. L. Santella, E. D. Specht, A. Rar, J. Frafjord, P. Rack, and J. Fowlkes, "Development of Combinatorial Methods for Alloy Design and Optimization," ASM Materials Solution Conference and Show, Columbus, Ohio, October 2004.

E. D. Specht, A. Rar, G. M. Pharr, P. D. Rack, E. P. George, J. D. Fowlkes, H. Hong, and E. Karapetrova, "Rapid Analysis of Ternary Phase Diagrams Using Synchrotron X-ray Diffraction and Fluorescence," 3rd Japan-U.S. Workshop on Combinatorial Materials Science and Technology, Okinawa, Japan, December 2004.

D. A. Smith, Y. Deng, J. D. Fowlkes, P. D. Rack, G. M. Pharr, L. H. VanBebber, F. Liu, C. L. Chiang, J. Wu, P. K. Liaw, and C. T. Liu "Thin Film Synthesis of BMG Alloys for Coatings and Combinatorial Alloy Design," 4th International Conference on Bulk Metallic Glasses, Gatlinburg, TN, May 1–5, 2005.

6. References

[1] X.-D. Xiang, *Annu. Rev. Mater. Sci.* **29**, 149 (1999).

[2] E.W. McFarland and W.H. Weinberg, *Tibtech* **17**, 107 (1999).

[3] Y.-K. Yoo, F. Duewer, H. Yang, D. Yi, J.-W. Li, and X.-D. Xiang, *Nature* **406**, 704 (2000).

[4] R. B. van Dover, L. F. Schneemeyer, and R. M. Flemming, *Nature* **392**, 162 (1998).

[5] E. M. DaSilva and C. E. Terune, *IBM Tech. Disclosure Bulletin* **22**, 2922 (1979).

[6] J. J. Hanak and J. I. Gittleman, *Physica* **55**, 555 (1971).

[7] R. W. Cahn, "Materials Science: Rapid Alloy Assessment," *Nature* **410**, 643 (2001).

[8] J.-C. Zhao, *Adv. Eng. Mater.* **3**, 143 (2001).

[9] H. Yamauchi et al., *ISTEC Journal* **5**, 25 (1992).

[10] S. R. Hall and M.R. Harrison, *Chemistry in Britain*, 739, September 1994.

[11] M. Th. Cohen-Adad, M. Gharbi, C. Goutaudier, and R. Cohen-Adad, *J. Alloys and Compounds* **289**, 185 (1999).

[12] *Science* **277**, 474, 25 July 1997.

[13] E. P. George and R. L. Kennedy, pp. 225–258 in *Impurities in Engineering Materials: Impact, Reliability and Control,* ed. C. L. Briant (Marcel Dekker, New York, 1999).

[14] C. G. McKamey, E. P. George, C. T. Liu, J. A. Horton, C. A. Carmichael, R. L. Kennedy, and W. D. Cao, *Manufacturing of Nickel-Base Superalloys with Improved High-Temperature Performance*, C/ORNL95-0327 (Oak Ridge National Laboratory, Oak Ridge, Tenn., January 2000).

[15] C. G. McKamey, E. P. George, C. A. Carmichael, W. D. Cao, and R. L. Kennedy, in *Proc. 9th Intl. Conf. on Creep and Fracture of Engineering Materials and Structures,* ed. J. D. Parker (Swansea, Wales, 2001).

[16] E. P. George, S. S. Babu, S. A. David, and B. B. Seth, in *Proc. BALTICA V* (Helsinki, Finland 2001).

[17] A. P. Hammersley, *FIT20 V10.3 Reference Manual V4.0,* ESRF Internal Report No. ESRF98HA01T (ESRF, Grenoble, France, 1998).

[18] A. P. Hammersly, S. O. Svensson, M. Hanfland, A. N. Flitch, and D. Hausermann, *High Press. Res.* **14**, 235 (1996).

[19] Y.-Y. Chuang and Y. Y. Chang, *Metall. Trans. A* **18,** 733 (1987).

[20] W. P. Rees, B. D. Burns, and A. J. Cook, *J. Iron Steel Inst.* **162,** 325 (1949).

[21] B. Josson, *ISIJ International* **35,** 1415 (1995).

[22] C. E. Campbell, W. J. Boettinger, and U. R. Kattner, *Acta Materialia* **50,** 775 (2002).

[23] S.-L. Chen, S. Daniel, F. Zhang, Y. A. Chang, X.-Y. Yan, F.-Y. Xie, R. Schmid-Fetzer, and W. A. Oates, *Calphad* **26**, 175 (2002).

[24] "SSOL2—SGTE Solutions Database," v. 2.0 (provided by ThermoCalc Software), SGTE, 2002.

[25] *The SGTE Casebook: Thermodynamics at Work,* ed. K. Hack (Institute of Materials, London, 1996), p. 227.

[26] J. A. Oberteuffer and J. A. Ibers, *Acta Crystallogr.*, *Sect. B*: *Struct. Sci.* **26**, 1499 (1970).

[27] M. C. Simmonds, R. C. Newman, S. Fujimoto, and J. S. Colligon, *Thin Solid Films* **279**, 4 (1996).

[28] E. D. Specht, A. Rar, G. M. Pharr, E. P. George, P. Zschack, H. Hong, J. Ilavsky, *J. Mater. Res.* **18**, 2522 (2003).

[29] E. D. Specht, P. D. Rack, A. Rar, G. M. Pharr, E. P. George, and H. Hong, p. 45 in *Combinatorial and Artificial Intelligence Methods in Materials Science II,* vol. 804, ed. R. A. Potyrailo, A. Karim, Q. Wang, and T. Chikyow (Materials Research Society, Warrendale, Pa., 2003).

[30] B. E. Warren, *X-Ray Diffraction* (Dover, New York, 1990), p. 253.

[31] A. Rar, E. D. Specht, E. P. George, M. L. Santella, and G. M. Pharr, *J. Vac. Sci. Technol.* **A 22**, 1788 (2004).

[32] F. E. W. Wetmore and D. J. LeRoy, *Principles of Phase Equilibria* (McGraw-Hill, New York, 1951), p. 10.

[33] J.-C. Zhao, *J. Mater. Res.* **16**, 1565 (2001).

[34] J.-C. Zhao, M. R. Jackson, and L. A. Peluso, *Acta Materialia* **51**, 6395 (2003).

[35] "4pi Revolution User Guide," online at http://www.4pi.com/teksupport/Rev10online/ manual/ 0-start.htm.

[36] W. C. Oliver and G. M. Pharr, *J. Mater. Res.* **6**, 1564 (1992).

[37] D. R. Askeland, *The Science and Engineering of Materials,* 3rd ed. (PWS Publishing, Boston, 1994).

[38] W. Smith, *Structure and Properties of Engineering Alloys* (McGraw Hill, New York, 1978).